

Polarization-Density Patterns of Active Particles in Motility Gradients

Sven Auschra,^{1,*} Viktor Holubec,^{1,2,†} Nicola Andreas Söker,^{3,‡} Frank Cichos,^{3,§} and Klaus Kroy^{1,¶}

¹*Theory of Condensed Matter, Institute for Theoretical Physics, Leipzig University, 04103 Leipzig, Germany*

²*Charles University, Faculty of Mathematics and Physics, Department of*

Macromolecular Physics, V Holešovičkách 2, CZ-180 00 Praha, Czech Republic

³*Molecular Nanophotonics Group, Peter Debye Institute for Soft Matter Physics, Leipzig University, 04103 Leipzig, Germany*

(Dated: November 2, 2020)

The co-localization of density modulations and emerging particle polarization is a characteristic feature of active matter in the vicinity of motility gradients. It therefore provides a robust tool to detect intrinsic microscopic activity by mesoscale observations. We employ the active-Brownian-particle model to address the density and polarization profiles of a single Janus-type swimmer in the vicinity of an abrupt activity step. The derived results nicely agree with measurements of polarization and density modulations of a single hot microswimmer at a motility step presented in the accompanying experimental paper [1]. Qualitative similarities to interfacial properties at motility-induced phase separations are observed. We generalize the theoretical framework to situations where the swimmer's propulsion speed depends on its orientation. Theory results are discussed and explained within a simplified two-species model.

I. INTRODUCTION

The surging field of active matter [2–4] aims for a microscopic understanding and control of the material properties of assemblies of interacting elements actively consuming energy [5]. Examples of active matter are ubiquitous in nature, ranging from flocks of birds [6], via swarms of insects [7] to bacteria such as *Escherichia coli* [8]. Furthermore, a wide range of laboratory studies ([5], Tab. I) has been devoted to suspensions of inanimate active particles or microswimmers, e.g. propelled by a form of self-phoretic motion [9–15], also called active fluids. Whether biological or artificial, one main task of physics is to develop tractable (toy) models that can closely mimic the distinctive traits of active matter.

On one hand, physical modelling aimed at a better understanding and characterization of types of activity and propulsion of individual active particles [9–17] and their interactions upon mutual encounters [18–20], encounters with walls [21, 22] or when exposed to external fields [23–27]. On the other hand, a huge body of simulations and theories (e.g., [4, 6, 28–46]) has aimed at the emerging collective properties of very large assemblies of active particles. There, the main strategy was to generalize established many-body theories in order to elucidate the new physics arising from nonequilibrium character of active matter and possibly unusual interactions of its active, autonomous “atoms”. On a coarse-grained level, passive particles and swimmers merely differ by hydrodynamic boundary conditions at their (coarse-grained) surfaces [47, 48]. But these can give rise to significant

differences that are usually lost in averaging by many-body theories [49].

What distinguishes active from passive matter on a fundamental level is the positive entropy production rate in the former [10, 50–65], measuring deviations from equilibrium [66–71]. Since the entropy production rate is commonly hardly accessible, the intrinsic activity is usually detected by mesoscopic measures, which offer a greater tangibility. Some of them are sufficient but not necessary (e.g., the occurrence of persistent ring currents [33], entropy generation on the trajectory level [72], or mesoscopic action-reaction symmetry breaking [28, 34]). Others suffer from the opposite limitation. Concerns arise, for instance, regarding the boundary-layer formation at (effectively) inelastic walls [35–37]. Those may already be caused by the interference of a curved boundary with persistent paths. It is therefore also observed for confined isothermal semiflexible polymers, for example [73]. Related concerns apply to the phenomenon of motility induced phase separation (MIPS) [43, 44, 74–78]. A variety of mechanisms for their occurrence, such as self-blocking of particles [79, 80], the existence of a non-equilibrium chemical potential [76, 77], or effective particle attractions [45] have been put forward. However, MIPS is arguably closely related to the well-known phenomenon of inelastic collapse in granular flows, which is a direct consequence of dissipative particle collisions [81, 82].

A property that has so far received relatively little attention is the emerging polarization-density pattern, which active matter displays in the vicinity of local motility variations. We claim that it is an inherent feature of intrinsic microscopic activity and provides, on a coarse-grained level, a robust criterion for the detection of active matter in a broad range of conceptually and practically relevant systems. We employ the active-Brownian-particle (ABP) model [4, 31, 83] to address the density and polarization profiles of a single Janus-type [9–17] swimmer in the vicinity of an abrupt activity step, which

* sven.auschra@itp.uni-leipzig.de

† viktor.holubec@mff.cuni.cz

‡ ns66qoxa@studserv.uni-leipzig.de

§ cichos@uni-leipzig.de

¶ klaus.kroy@itp.uni-leipzig.de

may be thought of as a concomitant feature of most physical boundaries (e.g., sedimentation [84–87], wall adsorption [35–37, 88] and MIPS interfaces [43, 44, 76, 77, 88–90]). Our analytical theory transcends and improves previous literature results [46, 91–93], and suggests itself as a practical numerical tool for the approximate reconstruction of the full picture from incomplete and coarse-grained active-particle data for more complex geometries and interacting many-body problems.

Outline: In Sec. II we briefly describe the experimental setup we used to study the dynamics of an active swimmer under sudden change of its swim speed. Our experimental findings and how they compare to our theoretical model are described in the accompanying letter [1] published alongside this article. Section II serves as a motivation for the theoretical framework we develop in section III. Applying the second order moment expansion of the space-and-angle dependent density in the ABP model, we derive a closed set of two approximate moment equations for the steady-state probability density ρ to find the particle at some position and its polarization \mathbf{p} at that point. After that, we explicitly calculate the density and polarization profiles for a quasi-onedimensional planar activity step. Expressions for typical sizes of polarization layers and bulk density ratios are derived. We then qualitatively compare the polarization and density profiles to those observed for MIPS. To check the consistency of our theoretical framework, we verified that the total polarization of the system [88] is determined by bulk fluxes. In order to address experimental observations at nudging interfaces [94–96], we also analytically calculate the corresponding polarization and density profile.

Section IV is dedicated to the physical interpretation of our results for the density and polarization profiles at various interfaces (active, passive, nudging). Our findings at onedimensional space-dependent motility landscapes are qualitatively captured within a simple, exactly solvable, 2-species model [65, 91, 92] that only admits two particle orientations. For orientation-independent activities, there actually exists an exact mapping between our approximate analytical theory and the 2-species model. We argue that this mapping onto a physically reasonable toy model explains the reliable results delivered by our theory regardless particle activities and also the fact that including the next term in the moment expansion actually leads to erroneous predictions for intermediate and large activities. For more complex geometries and/or orientation dependent activities, the mapping breaks down. But also in these cases the two species model serves as a reliable tool for sanity checks of results obtained using the approximate theory. We conclude in section V.

II. SETUP AND EXPERIMENTS

Experimentally, extensive single-particle measurements of an autonomous self-thermophoretic Janus type microswimmer [97] have been conducted [1] in a well-

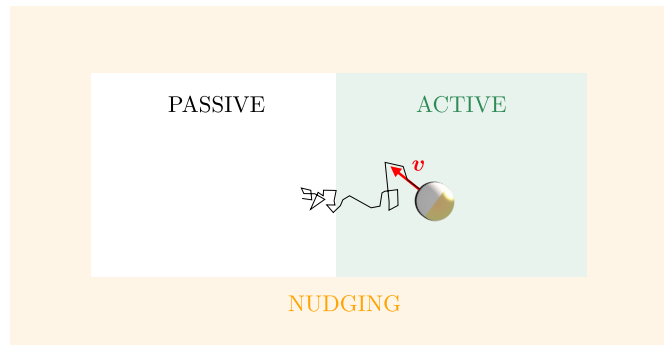


FIG. 1. Sketch of the experimental setup (not to scale). A single $1.5\mu\text{m}$ self-thermophoretic Janus swimmer is placed within a liquid film of $2.4\mu\text{m}$ thickness. The swimmer’s in-plane orientation and position are observed from top view in an inverted microscopy setup [1]. The particle propels actively with velocity \mathbf{v} whenever it is situated inside the ACTIVE area, otherwise the heating laser is switched off. To keep the particle inside the prescribed ACTIVE or PASSIVE areas, the Photon Nudging technique is applied [95, 96].

controlled setup, which is sketched in Fig. 1.

The motion of the self-thermophoretic Janus particle was controlled using a 532 nm laser. Undergoing permanent Brownian motion due to thermal fluctuations, upon laser irradiation, the Janus particle propels actively along its symmetry axis [9, 98]. The heating laser illuminates the whole sample area homogeneously and the polarization effects caused by variations of the laser intensity over the Janus particle [23, 24] are thus negligible. The particle translates and rotates within a $2.4\mu\text{m}$ water film, which is bounded by two cover slides. From aerial view of the sample (see Fig. 1), the Janus particle’s in-plane position and orientation are observed using an inverted microscope under darkfield illumination. Within the rectangular arena of roughly $6\mu\text{m} \times 5\mu\text{m}$, enclosed by the nudging region, the swimmer displays active propulsion if situated inside the active area on the right, otherwise the heating laser is switched off.

The measurements are made possible by the long-term confinement of the microswimmer within a dedicated “non-invasive” particle trap. We therefore employ the versatile technique of photon nudging [94–96, 98], which exploits the particle’s own self-propulsion in a Maxwell-demon type fashion. It enables us to realize a setup that is entirely force-free. Whenever the Janus particle exceeds the boundaries of the arena, the heating laser is switched off until the swimmer re-orientates back towards the arena, by virtue of rotational Brownian motion. Then the laser is switched on and the particle is “nudged” back into the arena.

Based on this experimental setup, we develop an approximate theoretical framework capable of reproducing the measured density and polarization profiles at the motility step qualitatively and, to a decent degree, also quantitatively.

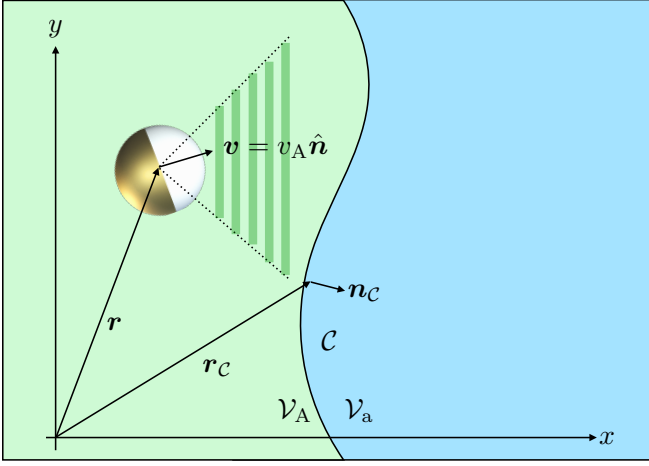


FIG. 2. Twodimensional sketch of a Janus particle with orientation $\hat{\mathbf{n}}$ and position \mathbf{r} . The system is divided into two subregions, $\mathcal{V}_{A,a}$, where the particle propels at distinct swim speeds, $v_{A,a}$. A restricted acceptance range of particle orientation (photon nudging) might also influence its activity, as indicated by the shaded area. The interface \mathcal{C} between the regions $\mathcal{V}_{A,a}$ is parametrized by the vector \mathbf{r}_C . And the corresponding normal vector \mathbf{n}_C points towards \mathcal{V}_a .

III. THEORY

A. Moment Equations

Experimental findings can be rationalized by the ABP model [4, 31, 83]. We consider an overdamped Janus swimmer in $d = 2, 3$ dimensions, whose propulsion speed $v(\mathbf{r}, \hat{\mathbf{n}})$ depends on its position \mathbf{r} and, in general, also on its orientation $\hat{\mathbf{n}}$. The particle's dynamics is modelled by the Langevin equations

$$\partial_t \mathbf{r} = v(\mathbf{r}, \hat{\mathbf{n}}) \hat{\mathbf{n}} + \sqrt{2D} \boldsymbol{\xi}_t, \quad \partial_t \hat{\mathbf{n}} = \sqrt{2D_r} \boldsymbol{\xi}_r \times \hat{\mathbf{n}}. \quad (1)$$

Here, D and D_r are the diffusion coefficients corresponding to the independent, unit variance, unbiased Gaussian white noise processes $\boldsymbol{\xi}_{t,r}(t)$ pertaining to the particle's translation and rotation, respectively. A sketch of the considered setup is presented in Fig. 2 for a piecewise constant activity profile in two spatial dimensions. Note that our theoretical model does not account for the so-called hot Brownian motion [99, 100], which a heated Janus particle generally performs by virtue of its non-isothermal environment.

The temporal evolution of the dynamic probability density $f(\mathbf{r}, \hat{\mathbf{n}}, t)$ for finding the Janus swimmer at time t at position \mathbf{r} with the orientation $\hat{\mathbf{n}}$ is described by the Fokker-Planck equation (FPE) [31, 83]

$$\partial_t f = D \nabla^2 f + D_r \nabla_n^2 f - \nabla [f v(\mathbf{r}, \hat{\mathbf{n}}) \hat{\mathbf{n}}]. \quad (2)$$

Here, ∂_t denotes the partial time derivative, and ∇^2 and ∇_n^2 are Laplace operators with respect to the positional and orientational variables, respectively. We truncate the

exact moment expansion of f with respect to the orientation $\hat{\mathbf{n}}$ as [83, 101, 102]

$$f(\mathbf{r}, \hat{\mathbf{n}}, t) = \frac{1}{S_d} [\rho(\mathbf{r}, t) + d \mathbf{p}(\mathbf{r}, t) \cdot \hat{\mathbf{n}}], \quad (3)$$

where we defined

$$S_d \equiv \int d\hat{\mathbf{n}} \quad (\text{unit sphere surface}), \quad (4)$$

$$\rho(\mathbf{r}) \equiv \int d\hat{\mathbf{n}} f(\mathbf{r}, \hat{\mathbf{n}}) \quad (\text{density}), \quad (5)$$

$$\mathbf{p}(\mathbf{r}) \equiv \int d\hat{\mathbf{n}} \hat{\mathbf{n}} f(\mathbf{r}, \hat{\mathbf{n}}) \quad (\text{polarization}). \quad (6)$$

Note that the moment expansion of f with respect to its angular degrees of freedom is not systematic with respect to a small parameter. Truncating the series expansion after the first two terms is physically motivated as the moment equations for $\rho(x)$ and $p(x)$ derived in Sec. III C for onedimensional activity profiles can be mapped onto an exact run-and-tumble model, which captures the relevant physics for arbitrary activity profiles (see Sec. IV A). Motivated by the experimental setup, the activity profile is modelled as $v(\mathbf{r}, \hat{\mathbf{n}}) = v(\mathbf{r}) \chi_{\mathcal{A}}(\hat{\mathbf{n}})$. Here, $v(\mathbf{r})$ reflects the occurrence of inhomogeneous activity in position space, and the indicator function $\chi_{\mathcal{A}}(\hat{\mathbf{n}})$ respects the fact that the particle might only propel actively if its orientation lies within a certain acceptance range \mathcal{A} . That is, $\chi_{\mathcal{A}}(\hat{\mathbf{n}}) = 1$ if $\hat{\mathbf{n}} \in \mathcal{A} \subseteq S_d$ and zero otherwise. This enables us to also model the technique of photon nudging.

Multiplying Eq. (2) by 1 or $\hat{\mathbf{n}}$, using $\nabla_n^2 \mathbf{n} = -(d-1)\mathbf{n}$, and integrating the result over orientational degrees of freedom, we obtain the following two moment equations [103]

$$\partial_t \rho(\mathbf{r}, t) = -\nabla \cdot \mathbf{J}(\mathbf{r}, t), \quad (7)$$

$$\partial_t \mathbf{p}(\mathbf{r}, t) = -(d-1)D_r \mathbf{p}(\mathbf{r}, t) - \nabla \cdot \mathbf{M}(\mathbf{r}, t). \quad (8)$$

Here, we introduced the (orientation-averaged) flux

$$\mathbf{J}(\mathbf{r}, t) \equiv -D \nabla \rho(\mathbf{r}, t) + v(\mathbf{r}) \left[\mathcal{I}_\rho^{(1)} \rho(\mathbf{r}, t) + \mathcal{I}_p^{(1)} \mathbf{p}(\mathbf{r}, t) \right], \quad (9)$$

and the matrix flux

$$\mathbf{M}(\mathbf{r}, t) \equiv -D \nabla \mathbf{p}(\mathbf{r}, t) + v(\mathbf{r}) \left[\mathcal{I}_\rho^{(2)} \rho(\mathbf{r}, t) + \mathcal{I}_p^{(2)} \mathbf{p}(\mathbf{r}, t) \right]. \quad (10)$$

The quantities $\mathcal{I}_{\rho,p}^{(1,2)}$ reflect the possibly restricted acceptance range \mathcal{A} of the heating laser, and are defined as

$$\begin{aligned} \mathcal{I}_\rho^{(1)} &\equiv \frac{1}{S_d} \int_{\mathcal{A}} d\hat{\mathbf{n}} \hat{\mathbf{n}}, \\ \mathcal{I}_p^{(1)} = d \mathcal{I}_\rho^{(2)} &\equiv \frac{d}{S_d} \int_{\mathcal{A}} d\hat{\mathbf{n}} \hat{\mathbf{n}} \hat{\mathbf{n}}, \\ \mathcal{I}_p^{(2)} &\equiv \frac{d}{S_d} \int_{\mathcal{A}} d\hat{\mathbf{n}} \hat{\mathbf{n}} \hat{\mathbf{n}} \hat{\mathbf{n}}. \end{aligned} \quad (11)$$

Note that for no orientational restriction of the heating laser, i.e., $\mathcal{A} = \mathcal{S}_d$ and $\chi_{\mathcal{A}} = 1$, the only contributing terms of the above integrals are

$$\mathcal{I}_p^{(1)} = d \mathcal{I}_p^{(2)} = \mathbf{1}, \quad (12)$$

with the unit matrix $\mathbf{1}$.

B. Steady State and Continuity Conditions

Throughout the rest of this article, we will restrict our considerations to the steady-state density and polarization. Setting the time-derivatives in Eqs. (7) and (8) to zero, we obtain

$$D \nabla^2 \rho(\mathbf{r}) = \nabla \cdot \left[v(\mathbf{r}) \left(\mathcal{I}_\rho^{(1)} \rho(\mathbf{r}) + \mathcal{I}_p^{(1)} \mathbf{p}(\mathbf{r}) \right) \right] \quad (13)$$

$$D \nabla^2 \mathbf{p}(\mathbf{r}) = (d-1) D_r \mathbf{p}(\mathbf{r}) + \nabla \cdot \left[v(\mathbf{r}) \left(\mathcal{I}_\rho^{(2)} \rho(\mathbf{r}) + \mathcal{I}_p^{(2)} \mathbf{p}(\mathbf{r}) \right) \right]. \quad (14)$$

Furthermore, it turns out that for all setups considered here the no-flux boundary conditions imply that the steady state flux $\mathbf{J}(\mathbf{r})$ vanishes at each point in space. Equation (9) then implies

$$\nabla \rho = \frac{v}{D} \left(\mathcal{I}_\rho^{(1)} \rho + \mathcal{I}_p^{(1)} \mathbf{p} \right), \quad (15)$$

which we substitute into Eq. (14).

Let us now consider two domains of constant activity, \mathcal{V}_A and \mathcal{V}_a , whose interface is described by a hyperplane \mathcal{C} , as sketched in Fig. 2. For $\mathbf{r} \in \mathcal{V}_{A,a}$, the Janus particle propels at constant swim speed $v_{A,a}$, given that its orientation lies within the acceptance range of the heating laser. Upon crossing the interface \mathcal{C} , the swimmer experiences a sudden change in its activity. The respective solutions $\rho_{A,a}(\mathbf{r})$ and $\mathbf{p}_{A,a}(\mathbf{r})$ of the steady-state moment Eqs. (13) and (14) within each domain $\mathcal{V}_{A,a}$ have to be correctly matched at the interface \mathcal{C} . Besides continuity of ρ and \mathbf{p} itself, we demand the normal components $\mathbf{J} \cdot \mathbf{n}_C$ and $\mathbf{M} \cdot \mathbf{n}_C$ of both fluxes to be continuous at each point \mathbf{r}_C along the interface \mathcal{C} [104]. Without loss of generality, the surface normal \mathbf{n}_C is defined to point towards \mathcal{V}_a . Computing the limits $\lim_{\epsilon \rightarrow 0} r_C \pm \epsilon$ in Eqs. (9) and (10) delivers the following two continuity conditions

$$\mathbf{n}_C \cdot (\mathbf{J}_a - \mathbf{J}_A) = 0, \quad \mathbf{n}_C \cdot (\mathbf{M}_a - \mathbf{M}_A) = 0. \quad (16)$$

The former relation is trivially obeyed by virtue of the no-flux condition $\mathbf{J} \equiv \mathbf{0}$. Both these conditions can also be obtained by integrating the (stationary) moment Eqs. (13) and (14) over an infinitesimal area around some point on the interface \mathcal{C} and exploiting the divergence theorem.

In the next section, we discuss analytical solutions for the density ρ and polarization \mathbf{p} for a quasi-one-dimensional system.

C. Planar activity step

Consider a situation in which the Janus swimmer faces an orientation-independent activity with a step at an infinite planar interface in $d = 2$ dimensions. For $x < x_a$, the particle propels at a swim speed v_A , which abruptly reduces to $v_a < v_A$ upon crossing the interface at $x = x_a$. Due to the translational symmetry of the system in the y -direction, we project the particle dynamics onto the x -axis by replacing $(\mathbf{r}, \hat{\mathbf{n}})$ by $(x, \cos \theta)$ in the general equations above.

In this situation, the only non-zero coefficients (11) are given by Eq. (12) and thus the flux balance (15) reads

$$\rho'(x) = \frac{v(x)}{D} \rho(x). \quad (17)$$

Plugging this relation into the moment Eq. (14) yields

$$p''(x) = \frac{p(x)}{\lambda^2(x)} + \frac{v'(x)\rho(x)}{2D}, \quad (18)$$

where we defined the natural relaxation length

$$\lambda(x) \equiv \left[\frac{D_r}{D} + \frac{v^2(x)}{2D^2} \right]^{-1/2}. \quad (19)$$

For the considered piecewise constant activity profile, Eq. (18) boils down within each halfspace to $p''_{A,a}(x) = p_{A,a}(x)/\lambda_{A,a}^2$ with the characteristic length scales $\lambda_{A,a}$ defined by Eq. (19). They are related as

$$\frac{\lambda_A}{\lambda_a} = \sqrt{\frac{1 + \mathcal{P}_a}{1 + \mathcal{P}_A}}, \quad \mathcal{P}_{A,a} \equiv \frac{v_{A,a}^2}{2DD_r}, \quad (20)$$

with the Péclet numbers $\mathcal{P}_{A,a}$ comparing active and diffusive transport rates in the respective halfspaces.

The general solutions of the polarization profiles are given by

$$p_{A,a}(x) = C_{A,a}^{(1)} e^{x/\lambda_{A,a}} + C_{A,a}^{(2)} e^{-x/\lambda_{A,a}} \quad (21)$$

and the density profile can be obtained by integrating Eq. (17) from an arbitrary reference point x_0 :

$$\rho(x) = \rho(x_0) + \int_{x_0}^x dx \frac{v(x)}{D} \rho(x). \quad (22)$$

The boundary term $\rho(x_0)$ follows from normalization condition on the density and the integration constants $C_{A,a}^{(1,2)}$ are determined by boundary and matching conditions at the activity step. The latter ones read

$$\rho_A(x_a) = \rho_a(x_a), \quad p_A(x_a) = p_a(x_a), \quad (23)$$

$$p'_a(x_a) - p'_A(x_a) = \frac{\rho_{A,a}(x_a)}{2D} (v_a - v_A), \quad (24)$$

where the second line follows from Eq. (16) while using $v'(x) = (v_a - v_A)\delta(x - x_a)$, with the delta function $\delta(x)$.

1. Natural boundaries

We first consider the situation with activity step at the origin, $x_a = 0$, and natural boundaries [105], i.e., $p(|x| \rightarrow \infty) = 0$. The continuity condition (23) then implies that the polarization profile in the respective halfspaces takes the form

$$p_{A,a}(x) = p_{\max} e^{-|x|/\lambda_{A,a}}, \quad (25)$$

with an unknown maximum polarization p_{\max} . The density profile follows via Eq. (22) as

$$\rho_A(x) = \rho_A + \frac{p_{\max}}{D} v_A \lambda_A e^{x/\lambda_A} \quad (26)$$

$$\rho_a(x) = \rho_A + \frac{p_{\max}}{D} (v_A \lambda_A + v_a \lambda_a - v_a \lambda_a e^{-x/\lambda_a}), \quad (27)$$

where we chose a reference point $x_0 \rightarrow -\infty$ at which ρ attains the constant bulk density ρ_A associated with the negative halfspace. The corresponding bulk density ρ_a in the positive halfspace is formally reached in the limit $x \rightarrow \infty$.

As an order parameter for the polarization at the interface, we define the relative maximum polarization $p_{\max}/\rho(0)$. The condition (24) allows to express it as

$$\frac{p_{\max}}{\rho(0)} = \frac{v_A - v_a}{2D} \frac{\lambda_A \lambda_a}{\lambda_A + \lambda_a} = \frac{1}{\sqrt{2}} \frac{\sqrt{\mathcal{P}_A} - \sqrt{\mathcal{P}_a}}{\sqrt{1 + \mathcal{P}_A} + \sqrt{1 + \mathcal{P}_a}}. \quad (28)$$

The sign of the relative maximum polarization and, via Eq (25), also that of the whole polarization profile $p(x)$ is solely determined by the difference in the swim speeds $v_A - v_a$. The Janus swimmer's thus on average points from the more into the less active region. The maximum $1/\sqrt{2}$ of $|p_{\max}|/\rho(0)$ is reached for $\mathcal{P}_A \rightarrow \infty$ and $\mathcal{P}_a = 0$ (or vice versa). It is smaller than 1 because we consider a two-dimensional motion projected onto the x -axis.

With Eqs. (26)–(28), the ratios $p_{A,a}(x)/\rho(0)$ and $[\rho(x) - \rho_A]/\rho(0)$ are uniquely determined. As detailed in App. A 1, the bulk density ratio can be shown to obey the relation

$$\frac{\rho_a}{\rho_A} = \frac{\lambda_a}{\lambda_A} = \sqrt{\frac{1 + \mathcal{P}_A}{1 + \mathcal{P}_a}}. \quad (29)$$

In section III C 3, we will show that this result is very general since it also holds for the full model (2) with arbitrary activity profiles mediating between the two bulk states.

In Fig. 3, we plot the approximate theory profiles following from Eqs. (25)–(29) and compare them to the (exact) numerical solutions obtained using the method of Ref. [106] from Eq. (2). In the figure, we considered the two cases $0 < v_a < v_A$ and $v_a = 0$ while $v_A > 0$. The characteristic length scales λ_i , bulk densities ρ_i and Péclet numbers \mathcal{P}_i corresponding to the highly

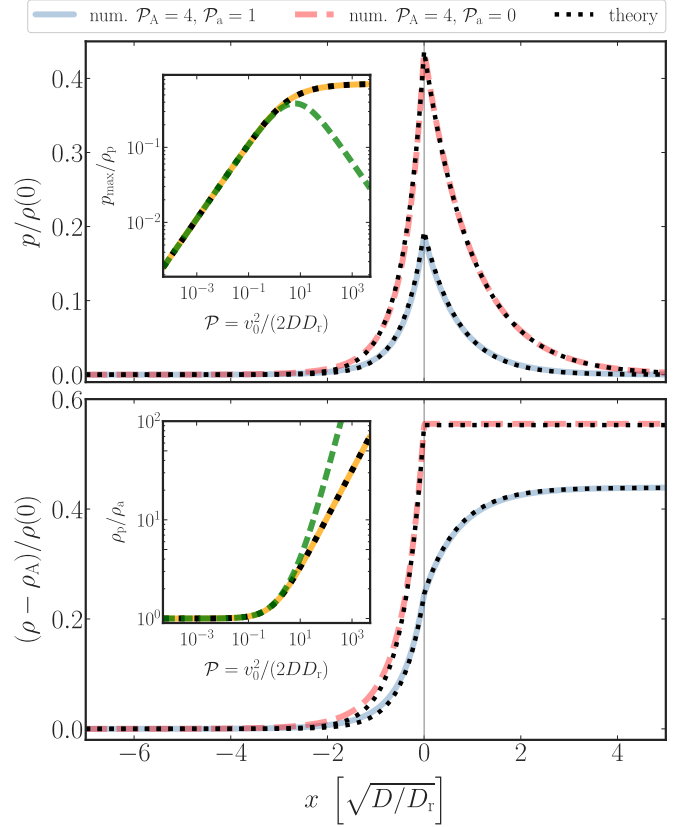


FIG. 3. Exact numerical solutions [106] for density and polarization profiles compared to approximate theory. The activity step is located at $x = 0$ [left: high activity (A), right: less active (a)/passive (p)]. Lengths are measured in units of $\sqrt{D/D_r}$ and velocities in units of $\sqrt{2DD_r}$. This corresponds to a dimensionless description of theory profiles [Eq. (25) and (28)] in terms of the corresponding Péclet number \mathcal{P}_i within each region. *Upper panel:* Reduced polarization $p/\rho(0)$; the theoretical curve was rendered using Eqs. (25) and (28). The inset figure shows the reduced polarization peak [relative to the bulk density in the passive region $\rho_p \equiv \rho(0)$] at an active-passive interface as function of the Péclet number \mathcal{P} of the active halfspace. Our theory curve (black dotted) calculated via Eq. (28) precisely follows the exact numerical solutions (solid line) and improves previous results of Ref. [93] (dashed line). *Lower panel:* The corresponding ratio $(\rho - \rho_A)/\rho(0)$ (ρ_A : bulk density in region of high activity) versus theory using Eqs. (26)–(28). The inset depicts the density ratio ρ_p/ρ_a for an active-passive interface ($\rho_{a,p}$: bulk densities in active/passive region) as a function of the Péclet number \mathcal{P} . Numerical results (solid line) are compared to Eq. (29) (dotted line), which improves the prediction of Ref. [93] (dashed line).

active ($x < 0$) and less active/completely passive regions ($x \geq 0$) are denoted by the subscripts (A), (a) and (p), respectively. In both main panels, the analytic solutions for the polarization and density profiles nicely agree with the numerical solutions with slight deviations present on the more active side.

Receiving reliable results from the approximate model

up to such a high degree of activity remains remarkable, as one intuitively would have guessed the approximation (3) to hold for $\mathcal{P} \ll 1$ only. We conjecture that this originates in the fact that the moment equations (17) and (18), pertaining to the approximate model, can be mapped onto an exactly solvable 2-species model (1D run-and-tumble [79, 91, 107] accompanied by diffusion [65, 92]; see Sec. IV A), which captures the relevant physics at the motility step for arbitrary Péclet numbers. Indeed, the quantitative agreement between approximate analytical and the exact (numerical) profiles remains very good up to Péclet numbers on the order of 100, as discussed in Ref. [108]. For even larger activities, higher moments in the moment expansion (3) become non-zero. However, employing the moment expansion up to the third order actually leads to less precise numerical predictions than our second-order approximation already for intermediate Péclet numbers on the order of 5.

From the upper panel, we infer that the relative polarization $p_{\max}/\rho(0)$ peaks exactly at the motility step with a magnitude given by Eq. (28), which improves the predictions of Ref. [93] (see inset). The polarization decays exponentially with the distance from the interface. The respective polarization layers extend over a characteristic length scale λ , which becomes narrower the higher the activity. Determined by Eq. (19), $\lambda \sim \sqrt{D/D_r}$ for vanishing propulsion speed, whereas in the opposite limit $\lambda \sim v/(2D)$. Both limits will be physically interpreted in the discussion section IV. Lack of an analytic proof, the inset figure entails strong numerical evidence that Eq. (28) for the reduced polarization peak generally holds for arbitrarily large activity steps. The lower panel of Fig. 3 presents the corresponding density profiles. For the active-passive interface, the density profile remains constant at the bulk density $\rho = \rho_p$ throughout the whole passive region by virtue of Eq. (17). On crossing the interface, it decays to the bulk density $\rho_A < \rho_p$ pertaining to the active region over a length scale λ_A . In the case of finite activity in both regions ($0 < v_a < v_A$), the density still displays a kink at the interface, but decays towards its bulk density value $\rho_{a,A}$ over the length scales $\lambda_{a,A} > 0$ into both respective half spaces. The inset of the lower panel of Fig. 3 compares the analytical expression (29) for the bulk density ratio ρ_p/ρ_a at an active-passive interface with the exact numerical solution. Over a vast range of Péclet numbers \mathcal{P} , both curves perfectly overlap, indicating the validity of Eq. (29) also for the non-approximate model and thereby improving predictions by Ref. [93].

Before discussing these generalized scenarios, we comment on the potential of the presented framework to yield approximate analytical polarization-density patterns at various kinds of interfaces, e.g., hard walls. We also point out similarities between the well-known phenomenon of MIPS displayed by active-particle suspensions, and the polarization and density profiles found at a motility step. Finally, we address the topic of swim pressure and the closely related total polarization of a system.

2. Relation to wall accumulation, MIPS and swim pressure

Wall Accumulation: The Eqs. (17) and (18) can serve as a general tool to calculate (approximate) polarization and density profiles at various kinds of interfaces or boundaries since the latter enter the governing equations only via different boundary conditions. As a concrete example, Eqs. (17) and (18) might be applied to compute $p(x)$ and $\rho(x)$ of an active particle confined by hard walls, which are realized by reflecting boundary conditions [104]. Our model captures the well-known effects of polarization towards and accumulation at walls [35–37, 65, 88, 92]. The simplest way to obtain specific profiles is by exploiting the equivalence between the approximate model, Eqs. (17) and (18), and the 2-species model (see Sec. IV A), and compute $\rho(x)$ and $p(x)$ within the framework of the latter, which was done in [65, 92]. The respective polarization and density layers near the wall are still determined by the length scale λ in Eq. (19) and therefore undergo the same physics as those at motility steps (see the discussion section IV B).

MIPS: An extensively studied feature of active-Brownian-particle suspensions is their capability to display MIPS [43, 44, 74–78]. In a nutshell, its occurrence depends on two ingredients: (i) the slowing down of particles in “crowded” areas [91], and (ii) particle accumulation in slow areas [74]. Our results for the polarization and density profiles of a single (overdamped) Janus swimmer can, at least on a qualitative level, closely resemble the effects observed for MIPS if applied to a gas of non-interacting active Janus spheres experiencing an inhomogeneous activity profile, e.g. inversely proportional to the particle density in a system that display MIPS. As also pointed out in Ref. [108], such a gas exhibits the following features observed in MIPS:

- (i) The system divides into two bulk areas with different bulk densities. Particles move slower (faster) in the denser (less dense) regions [44, 74] (cf. Eq. (29) and lower panel of Fig. 3).
- (ii) An interfacial region forms between the two bulk areas, where particles, on average, point into the denser phase [44, 76, 77] (cf. upper panel of Fig. 3). Note that for active Lennard-Jones particles, an opposite polarization was observed [90].
- (iii) The smaller the activity on one side the larger the extend of the corresponding polarization layer [78] (cf. Eq. (19)).

One of the systems exhibiting MIPS are active particles adjusting their activity according to the local density via chemical signaling, e.g., quorum sensing [109]. In this case, Eq. (29) for the bulk density ratio can be used to improve the corresponding results of Ref. [93], where “Quorum-sensing active particles” are discussed within a dynamic mean-field theory.

Swim pressure/Total polarization: In suspensions of active Brownian particles a “swim pressure” [77, 110] emerges due to local polarization of the swimmers in the vicinity of various interfaces (sedimentation [84–87], walls [35–37, 88], MIPS [43, 44, 76, 77, 88–90]). The swim pressure is, up to a prefactor, determined by the total polarization P_{tot} , which is defined as the integrated local polarization profile p over some (sub-)volume [88], and thus also points from the more to the less active region. For the motility step considered in the previous section, Eqs. (25) and (29) imply that within our approximate model the total polarization reads

$$P_{\text{tot}} = \int_{-\infty}^{\infty} dx p(x) = p_{\text{max}}(\lambda_a + \lambda_A) = \frac{v_A \rho_A - v_a \rho_a}{2D_r}. \quad (30)$$

A derivation of the last equality is performed in the second part of App. A 1. The total polarization is thus determined by the difference of the bulk fluxes $v_{A,a} \rho_{A,a}$ in the respective halfspaces and the rotational diffusion coefficient D_r . This agrees with the general result of Hermann and Schmidt [88] and verifies that the total polarization induced by an activity step is a state function.

In the next subsection, we proof that Eq. (29) for the bulk density ratio actually holds for the full ABP model (2) and for arbitrary activity variations.

3. Density ratio

Consider an arbitrary activity profile $v(x)$ that mediates between two bulk regions of respectively constant activity. Using Eq. (2), the corresponding stationary FPE for the probability density $f(x, \theta)$ reads

$$0 = -\partial_x \mathcal{J} - \partial_\theta \mathcal{J}_\theta = D \partial_x^2 f + D_r \partial_\theta^2 f - \partial_x (v \cos \theta f), \quad (31)$$

where we have introduced the (angle-resolved) translational and rotational currents

$$\mathcal{J}(x, \theta) \equiv -D \partial_x f(x, \theta) + v(x) \cos \theta f(x, \theta), \quad (32)$$

$$\mathcal{J}_\theta(x, \theta) \equiv -D_r \partial_\theta f(x, \theta). \quad (33)$$

Instead of a truncation after two terms as in Eq. (3), we now consider the full expansion of f into the Fourier series

$$f(x, \theta) = \frac{\rho(x)}{2\pi} + \frac{1}{\pi} \sum_{n=1}^{\infty} f_n(x) \cos(n\theta), \quad (34)$$

with the coefficients $f_n = \langle \cos(n\theta) \rangle = \int_0^{2\pi} d\theta \cos(n\theta) f(x, \theta)$. In accord with our previous discussion, the zeroth and the first coefficients are given by the density $\rho \equiv \langle 1 \rangle$ and the polarization $p \equiv f_1 = \langle \cos \theta \rangle$, respectively. The orientation-averaged flux thus reads

$$J(x) \equiv \langle \mathcal{J}(x, \theta) \rangle = -D \rho'(x) + v(x) p(x). \quad (35)$$

We now multiply the FPE (31) by $\cos \theta$ and integrate over θ . This renders the differential equation for the polarization

$$0 = D p'' - D_r p - \frac{v}{2} \rho' - \frac{\rho}{2} v' - \partial_x (v f_2), \quad (36)$$

where we used the identity $2 \cos^2 \theta = 1 + \cos(2\theta)$. Note that the last term in Eq. (36) was absent in the previous discussions due to the applied closure relation $f_2 = \langle \cos(2\theta) \rangle = 0$. Transposing Eq. (36) for p and plugging it into Eq. (35) yields

$$J(x) = -D_{\text{eff}}(x) \rho'(x) - \frac{1}{2} \rho D_{\text{eff}}' + J_{v'}(x), \quad (37)$$

with the position-dependent effective diffusivity

$$D_{\text{eff}}(x) \equiv D + \frac{v^2(x)}{2D_r} \quad (38)$$

and the flux

$$J_{v'} \equiv \frac{D}{D_r} v(x) p''(x) + \frac{v}{D_r} \partial_x (v f_2). \quad (39)$$

Equation (37) constitutes a generalized version of Fick’s law. The first contribution $-D_{\text{eff}} \rho'$ accounts for omnidirectional transport via diffusion enhanced ($D_{\text{eff}} \geq D$) by the swimmer’s persistent motion. The second term, $\rho D_{\text{eff}}'/2$, describes the effect of the space dependency of the particle’s effective diffusivity and its prefactor $1/2$ originates from the directionality of the active velocity. The last contribution, $J_{v'}$, represents the influence of the polarization $p(x)$ and higher moments f_n , $n > 1$ on the local density.

The condition on vanishing steady-state flux, $J(x) = 0$, Eq. (37) yields

$$\frac{\rho'}{\rho} = -\frac{1}{2} \frac{D_{\text{eff}}'}{D_{\text{eff}}} + \frac{J_{v'}}{\rho D_{\text{eff}}}. \quad (40)$$

Integrating this equation from a reference point x_0 up to an arbitrary position x , we find

$$\frac{\rho(x)}{\rho(x_0)} = \sqrt{\frac{D_{\text{eff}}(x_0)}{D_{\text{eff}}(x)}} \exp \{ \mathcal{U}[v](x_0, x) \}, \quad (41)$$

where we introduced the functional

$$\mathcal{U}[v](x_0, x) \equiv \int_{x_0}^x d\tilde{x} \frac{J_{v'}(\tilde{x})}{\rho(\tilde{x}) D_{\text{eff}}(\tilde{x})}. \quad (42)$$

Equation (41) shows that density ratios are determined by the ratio of the corresponding effective diffusion coefficients, corrected by the exponential of a complicated functional $\mathcal{U}[v](x_0, x)$ of the $J_{v'}/D_{\text{eff}}$ and thus the activity profile $v(x)$. Equation (41) is therefore not suitable for calculation of the full density profile. However, if the integration bounds x_0 and x in (41) and (42) are sufficiently far away from the activity variations, such that

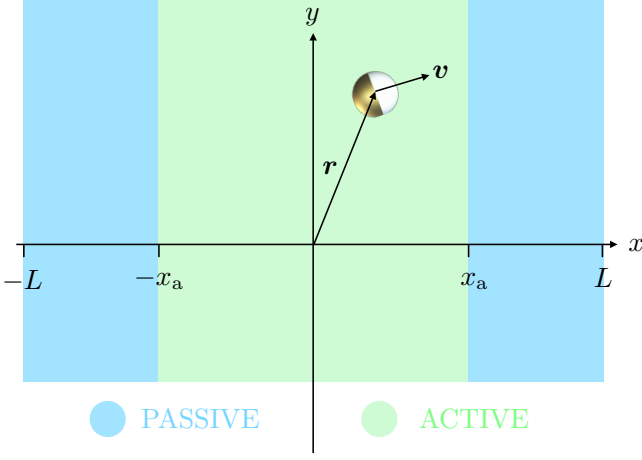


FIG. 4. Sketch of a Janus particle with orientation $\mathbf{n} = (\cos \theta, \sin \theta)$ and position $\mathbf{r} = (x, y)$. It propels actively with velocity $\mathbf{v} = v_0 \mathbf{n}$ along its symmetry axis as long as $|x| < x_a$. Otherwise it undergoes ordinary translational and rotational diffusion. The system has periodic boundaries located at $\pm L$.

$\rho(x)$ and $\rho(x_0)$ correspond to the bulk densities, one can prove that the functional $\mathcal{U}[v](x_0, x) = 0$, irrespective of the activity profile $v(x)$ (see App. A 2). We therefore find that bulk density ratios are generally related via

$$\frac{\rho(x)}{\rho(x_0)} = \sqrt{\frac{D_{\text{eff}}(x_0)}{D_{\text{eff}}(x)}}, \quad (43)$$

which, using the definition of the Péclet number on the r.h.s. of Eq. (19), coincides with Eq. (29). For highly persistent swimmers, i.e., $v^2(x) \gg 2DD_r$, Eq. (43) reduces to the well-known relation [103, 111] $\rho(x)/\rho(x_0) = v(x_0)/v(x)$. To conclude, the bulk density ratio $\rho(x)/\rho(x_0)$ is generally independent of the exact shape and magnitude of the activity variations. As a consequence, on a mesoscopic scale, at which all moments $f_{n>0}$ in Eq. (34) are negligibly small compared to ρ , the coarse-grained version of flux balance (37) reads $\bar{J}(x) = -D_{\text{eff}}(x)\rho'(x) - \frac{1}{2}\rho D_{\text{eff}}'$.

In the next paragraph, we derive specific expressions for $\rho(x)$ and $p(x)$ in a system of finite size. In the accompanying article [1], we show that these analytic solutions agree with experimentally determined profiles.

4. Finite system

We consider a system of length $2L$ composed of an active region of length $2x_a$, surrounded by two passive regions interconnected by periodic boundaries, see Fig. 4. The corresponding activity profile is given by $v(x) = v_0 \Theta(x_a - |x|)$. The symmetry of this setup allows us to consider only the positive half space with active-passive interface at $x = x_a$. The respective polarization and density profiles in the active and passive regions are

still given by Eqs. (21) and (22). By virtue of the system's symmetry and the imposed periodic boundary conditions at $x = \pm L$, the polarization must obey $p_a(0) = 0$ and $p_p(L) = 0$. Hence, the polarization profiles in the active and passive regions read

$$p_a(x) = C_a \sinh\left(\frac{x}{\lambda_a}\right), \quad p_p(x) = C_p \sinh\left(\frac{L-x}{\lambda_p}\right). \quad (44)$$

Taking $x_0 = 0$ as reference point in Eq. (22), the density profile on the active side ($0 \leq x < x_a$) reads

$$\rho_a(x) = \rho_a(0) + \frac{C_a v_0 \lambda_a}{D} \left[\cosh\left(\frac{x}{\lambda_a}\right) - 1 \right]. \quad (45)$$

The corresponding density profile on the passive side ($x_a \leq x \leq L$) is constant, $\rho_p(x) \equiv \rho_a(0)$. The integration constants C_a and C_p and the reference density $\rho_a(0)$ are uniquely determined by the continuity conditions

$$p_p(x_a) = p_a(x_a), \quad (46)$$

$$p_a'(x_a) - p_p'(x_a) = \frac{v_0}{2D} \rho(x_a), \quad (47)$$

and the normalization condition on $\rho(x)$. The detailed calculation is shown in App. A 3.

Here, we assume that the active and passive regions are sufficiently larger than the respective decay lengths $\lambda_{a,p}$ to avoid that the system is dominated by boundary physics. In this regime, the polarization and density profiles can be written as

$$p_a(x) = \frac{1}{2L} \frac{P_{\text{max}}}{1 - (1 - r_\rho) \frac{x_a - \lambda_a}{L}} \frac{\sinh(x/\lambda_a)}{\sinh(x_a/\lambda_a)}, \quad (48)$$

$$p_p(x) = \frac{1}{2L} \frac{P_{\text{max}}}{1 - (1 - r_\rho) \frac{x_a - \lambda_a}{L}} \frac{\sinh((L-x)/\lambda_p)}{\sinh((L-x_a)/\lambda_p)}, \quad (49)$$

$$\rho_a(x) = \frac{1}{2L} \left[\frac{1}{1 - (1 - r_\rho) \frac{x_a - \lambda_a}{L}} + \frac{1 - r_\rho}{1 - (1 - r_\rho) \frac{x_a - \lambda_a}{L}} \left(\frac{\cosh(x/\lambda_a)}{\sinh(x_a/\lambda_a)} - 1 \right) \right], \quad (50)$$

$$\rho_p(x) \equiv \rho_a(x_a) = \frac{1}{2L} \frac{1}{1 - (1 - r_\rho) \frac{x_a - \lambda_a}{L}}, \quad (51)$$

where we introduced the short-hands

$$P_{\text{max}} \equiv \frac{v_0}{2D} \frac{\lambda_a \lambda_p}{\lambda_a + \lambda_p} = \frac{1}{\sqrt{2}} \frac{\sqrt{\mathcal{P}}}{1 + \sqrt{1 + \mathcal{P}}}, \quad (52)$$

$$r_\rho \equiv \frac{\lambda_a}{\lambda_p} = \frac{1}{\sqrt{1 + \mathcal{P}}}, \quad (53)$$

for the maximum (relative) polarization and density ratio, respectively. In Fig. 5, we show that these results agree nicely with the (exact) numerical solutions [106]. In the accompanying paper [1], we further show that they also nicely describe the experimental data.

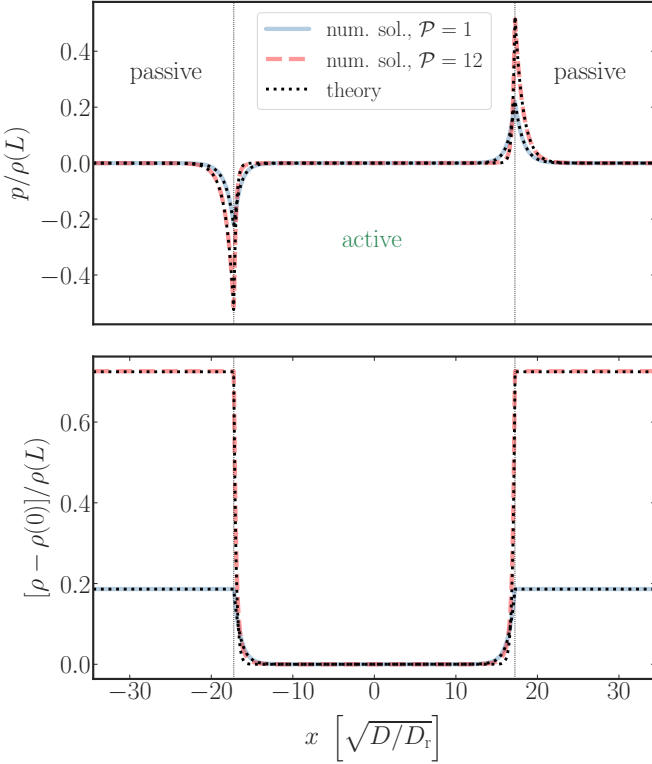


FIG. 5. Exact numerical solutions [106] for density and polarization profiles are compared to theory (48)-(51). Lengths and velocities are measured in units of $\lambda_p = \sqrt{D/D_r}$ and $\sqrt{2DD_r}$, respectively. The active-passive interfaces are located at $x = \pm 10 \lambda_p$, whereas the system boundaries are located at $\pm 20 \lambda_p$.

Note that the total polarization of the system in Fig. 5, $P_{\text{tot}} = \int_{-L}^L dx p(x)$, vanishes by virtue of the anti-symmetry between the polarization profiles on the left and right activity step. This is in agreement with Ref. [88] stating that $P_{\text{tot}} = 0$ for systems with vanishing fluxes at their boundary, which means that, in closed systems, the inhomogeneous activity profiles just operate as a spatial-sorting mechanism for particles of different polarisation.

In the next section, we allow the particle's activity to also depend on its orientation. This mimics the technique of photon nudging [94–96, 98] exploited in our experiments [1] to confine the Janus particle to the active-passive arena (see Fig. 1).

D. Photon-Nudging

In this section, we restrict the heating laser's acceptance range of particle orientations. The activity profile of the Janus swimmer is modelled as $v(x, \theta) = v(x)\Theta(\alpha - |\theta|)$, where α represents the acceptance angle of the laser. Then, the no-flux condition (15) and the

moment Eq. (14) take the form

$$\rho' = \frac{v}{D} \left(\mathcal{I}_\rho^{(1)} \rho + \mathcal{I}_p^{(1)} p \right) \quad (54)$$

$$p'' = \frac{D_r}{D} p + \frac{v}{D} \left(\mathcal{I}_\rho^{(2)} \rho' + \mathcal{I}_p^{(2)} p' \right) + \frac{v'}{D} \left(\rho \mathcal{I}_\rho^{(2)} + p \mathcal{I}_p^{(2)} \right). \quad (55)$$

According to the definitions (11), the constants $\mathcal{I}_{\rho,p}^{(1,2)}$, which represent the influence of the restricted acceptance angle α of the heating laser, read

$$\mathcal{I}_\rho^{(1)} = \frac{1}{2\pi} \int_{-\alpha}^{\alpha} d\theta \cos \theta = \frac{\sin \alpha}{\pi}, \quad (56)$$

$$\mathcal{I}_p^{(1)} = \frac{1}{\pi} \int_{-\alpha}^{\alpha} d\theta \cos^2 \theta = \frac{\alpha}{\pi} + \frac{\sin(2\alpha)}{2\pi}, \quad (57)$$

$$\mathcal{I}_\rho^{(2)} = \frac{\mathcal{I}_p^{(1)}}{2} = \frac{\alpha}{2\pi} + \frac{\sin(2\alpha)}{4\pi}, \quad (58)$$

$$\mathcal{I}_p^{(2)} = \frac{1}{\pi} \int_{-\alpha}^{\alpha} d\theta \cos^3 \theta = \frac{9 \sin \alpha + \sin(3\alpha)}{6\pi}. \quad (59)$$

The swimmer is nudged to the right if $\alpha < \pi$. Nudging to the left is captured by formally replacing $v \rightarrow -v$. The case $\alpha = \pi$ corresponds to a fully active swimmer, irrespective of its orientation. As in the previous sections, the particle faces a sudden activity change at $x = x_a \equiv 0$. Without loss of generality, the particle is nudged (n) to the right for $x \leq 0$. Upon crossing the boundary into the positive halfspace, it faces a fully active (a) or passive region (p), where its activity does not depend on orientation. Within each half space, the corresponding swim speed $v_i \geq 0$, $i \in \{n, a, p\}$, is constant. Plugging the steady-state condition (54) into the moment Eq. (55) yields an equation of the form

$$\mathbf{X}' = \mathbf{\Lambda} \mathbf{X}, \quad (60)$$

where we introduced

$$\mathbf{X} \equiv (p', p, \rho)^\top, \quad (61)$$

$$\mathbf{\Lambda} \equiv \begin{pmatrix} \frac{v_i}{D} \mathcal{I}_p^{(2)} & \frac{D_r}{D} + \frac{v_i^2}{D^2} \mathcal{I}_\rho^{(2)} \mathcal{I}_p^{(1)} & \frac{v_i^2}{D^2} \mathcal{I}_\rho^{(1)} \mathcal{I}_\rho^{(2)} \\ 1 & 0 & 0 \\ 0 & \frac{v_i}{D} \mathcal{I}_p^{(1)} & \frac{v_i}{D} \mathcal{I}_\rho^{(1)} \end{pmatrix}. \quad (62)$$

For $\alpha < \pi$, all the integrals $\mathcal{I}_{\rho,p}^{(1,2)}$ from Eqs. (56)-(59) give nonzero contributions. In App. B 1 we explicitly calculate the eigenvalues $\lambda_{n_i}^{-1}$ of the matrix $\mathbf{\Lambda}$. All of them are real and mutually distinct. The general solution to Eq. (60) thus has the structure

$$\mathbf{X} = \sum_{k=1}^3 C_i \mathbf{w}_i e^{\lambda_{n_i}^{-1} x}, \quad (63)$$

where \mathbf{w}_i denotes the eigenvector pertaining to the eigenvalue $\lambda_{n_i}^{-1}$. The coefficients C_i are determined by boundary and continuity conditions applying to the respective solutions at the interface. The intuitive relations at a nudging-active interface

$$\rho_n(0) = \rho_a(0), \quad p_n(0) = p_a(0), \quad (64)$$

are complemented by the continuity condition

$$p'_a(0) - p'_n(0) = \frac{v_a/2 - v_n \mathcal{I}_{\rho_n}^{(2)}}{D} \rho(0) - \frac{v_n \mathcal{I}_{p_n}^{(2)}}{D} p(0), \quad (65)$$

which follow from Eq. (16) while using that $I_{\rho_a}^{(2)} = 1/2$ and $I_{p_a}^{(2)} = 0$ within the active halfspace (see Eq. (12) and sentence above). Continuity equations for a nudging-passive interface follow by setting $v_a = 0$ in Eq. (65).

Given natural boundary conditions, we demand that the polarization vanishes for $x \rightarrow \pm\infty$. The density attains constant bulk values $\rho_n = 0$ and $\rho_{a,p} > 0$ in the nudging and active/passive bulk, respectively. Hence, inside the nudging region ($x \leq 0$), only eigenvalues $\lambda_{n_i}^{-1} > 0$ will contribute to the general solution (63). Since the analytical expressions for the eigenvalues $\lambda_{n_i}^{-1}$ are too complicated (see App. B1), we discuss their behavior graphically. The upper panel of Fig. 6 depicts the dependence of the eigenvalues $\lambda_{n_i}^{-1}$ on the propulsion velocity v measured in units of $\sqrt{2DD_r}$, i.e., in terms of the Péclet number \mathcal{P} , for two fixed values of the acceptance angle (dashed curves: $\alpha = 45^\circ$, solid curves: $\alpha = 90^\circ$). In the lower panel of Fig. 6, we plot the dependence of $\lambda_{n_i}^{-1}$ on the acceptance angle α for three fixed Péclet numbers (dotted curves: $\mathcal{P} = 1/2$, dashed curves: $\mathcal{P} = 1$, solid curves: $\mathcal{P} = 2$). In both panels, all eigenvalues are measured in units of the inverse characteristic length $\lambda_p^{-1} = \sqrt{D/D_r}$ of a passive boundary layer (cf. Sec. III C 1). From the main plot of the upper panel of Fig. 6, one infers that $\lambda_{n_1}^{-1} \geq \lambda_p^{-1}$ and $\lambda_{n_2}^{-1} \geq 0$, whereas the third eigenvalue is negative. This separation holds for all acceptance angles $0 \leq \alpha \leq \pi$ as can be seen from the lower panel of Fig. 6 (and the discussion in App. B3). Therefore, only $\lambda_{n_1}^{-1}$ and $\lambda_{n_2}^{-1}$ contribute to the general solution (63). In contrast to purely active-passive interfaces, which are characterized by a single natural length scale $\lambda_{a,p}$, there are thus always two characteristic lengths, λ_1 and λ_2 , that determine the shape of the polarization and density profiles within the nudging layer. Both $\lambda_{n_1}^{-1}$ and $\lambda_{n_2}^{-1}$ grow monotonously with increasing propulsion speed v ; $\lambda_{n_2}^{-1}$ much more gently, though. While $\lambda_{n_2}^{-1}$ remains strictly below the (inverse) natural length λ_a^{-1} of a fully active polarization layer, $\lambda_{n_1}^{-1}$ might even exceed it, depending on swim speed and the acceptance angle. For slow swim speeds, i.e., small \mathcal{P} , one generally has $\lambda_{n_1}^{-1} > \lambda_a^{-1}$, as detailed in App. B3. Purely active or passive polarization layers are captured within this framework (eigenvalues of matrix $\mathbf{\Lambda}$) as well. In the limiting case of vanishing activity ($v \rightarrow 0$), one finds $\lambda_{n_2}^{-1} \rightarrow 0$, which renders a constant contribution (bulk density) to the general solution

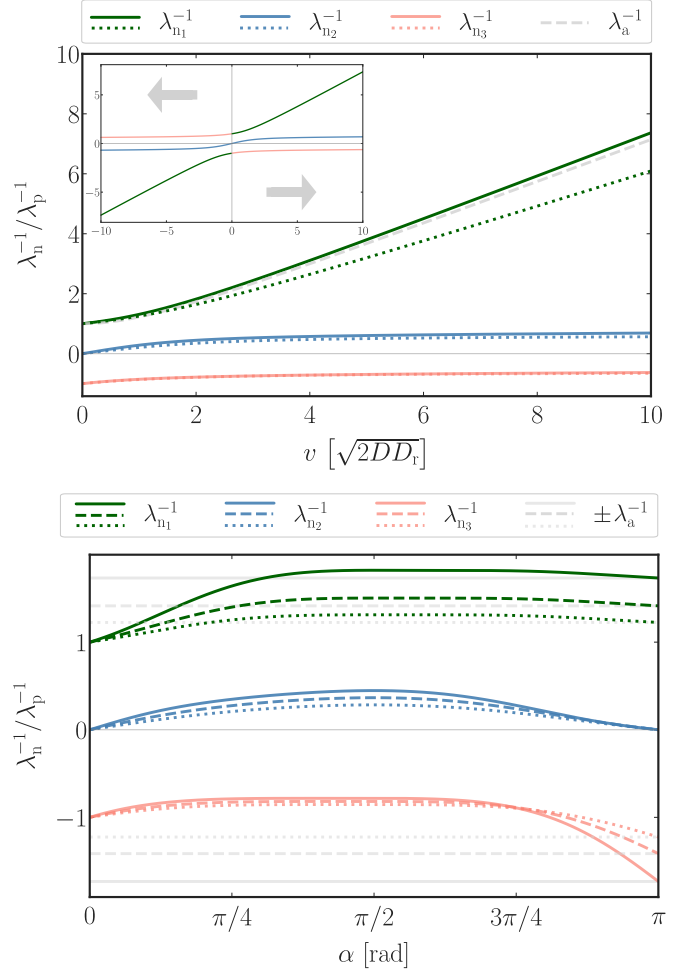


FIG. 6. Dependence of eigenvalues λ^{-1} on particle propulsion speed v and acceptance angle α of the heating laser. $\lambda_{n_i}^{-1}$, $i \in \{1, 2, 3\}$, denote the eigenvalues of the matrix $\mathbf{\Lambda}$ defined in Eq. (62). $\lambda_{a,p}^{-1}$ are the inverse characteristic length scales of an active/passive layer [Eq. (19)]. Upper panel: Eigenvalues were calculated for fixed acceptance angles $\alpha = 45^\circ$ (dotted curves) and $\alpha = 90^\circ$ (solid curves). Inset: Dependence of eigenvalues on nudging direction (indicated by gray arrows). Lower panel: Eigenvalues were calculated for the fixed Péclet numbers $\mathcal{P} \in \{1/2, 1, 2\}$ (dotted, dashed, solid curve).

(63), whereas $\lambda_{n_{1,3}}^{-1} \rightarrow \pm \lambda_p^{-1}$. The positive/negative sign refers to a polarization layer in the negative/positive halfspace. Only one of both eigenvalues contributes whereas the other vanishes by virtue of natural boundary conditions to ensure $p(|x| \rightarrow \infty) = 0$. Similarly, for a fully active region ($\alpha \rightarrow \pi$), the eigenvalues $\lambda_{n_{1,3}}^{-1}$ approach $\pm \lambda_a^{-1}$, which is indicated by the gray lines in the lower panel of Fig. 6. Here, positive/negative sign also refers to a polarization layer in the negative/positive halfspace. Only one of them contributes due to the boundary conditions. The eigenvalue $\lambda_{n_2}^{-1}$ vanishes and gives a constant contribution (bulk density) to the general solution (63). The inset of the upper panel of Fig. 6 contains information about the behavior of all three eigenvalues upon

inverting the direction of the nudging process. We find a completely symmetric picture when replacing $v \rightarrow -v$. Only the roles of the respective eigenvalues change, as we now only allow for negative eigenvalues to contribute (particles are nudged to the left if $x > 0$). So $\lambda_{n_1}^{-1}$ becomes $\lambda_{n_3}^{-1}$ and thus does not contribute to $p(x)$ and $\rho(x)$ anymore. Conversely, $\lambda_{n_3}^{-1} \rightarrow \lambda_{n_1}^{-1}$. The eigenvalue $\lambda_{n_2}^{-1}$ changes its sign upon inverting the direction of propulsion and thus keeps its role.

Having the eigenvalues $\lambda_{n_{1,2}}^{-1}$ and the corresponding eigenvectors $\mathbf{w}_{1,2}$ of matrix \mathbf{A} that contribute to the general solution (63), we obtained the polarization and density profiles in the case of a nudging-active as well as a nudging-passive interface. Polarization and density profiles are matched to those in the respective passive/active half space by the continuity conditions (64) and (65). The resulting profiles are depicted as black-dotted curves in Fig. 7 for $\mathcal{P} = 1$ in the vicinity of a nudging-passive (left plots) and a nudging-active interface (right plots). Both $p(x)$ and $\rho(x)$ were normalized by the bulk value $\rho_\infty \equiv \rho(x \rightarrow \infty)$ of the density inside the active/passive bulk, respectively. In all scenarios we considered two distinct acceptance angles, $\alpha = 45^\circ$ and 90° . All the approximate analytical solutions nicely follow the exact numerical results [106], which are represented by the blue ($\alpha = 45^\circ$) and red ($\alpha = 90^\circ$) curves. An intuitive understanding of the presented density and polarization profiles in terms of a 2-species model will be provided in Sec. IV C and IV D.

The lower panels of Fig. 7 depict the relative polarization profiles $p(x)/\rho(x)$ in both scenarios. Peaking exactly at the interface, p/ρ decays over a length scale $\lambda_{n_1} < \lambda_{n_2}$ into the nudging region (left) and approaches a constant nonzero value. The (relative) bulk polarization $(p/\rho)_n$ within the nudging region can be calculated explicitly. We therefore rewrite Eq. (54) as

$$\frac{p(x)}{\rho(x)} = \frac{D}{v(x)\mathcal{I}_p^{(1)}} \frac{\rho'(x)}{\rho(x)} - \frac{\mathcal{I}_p^{(1)}}{\mathcal{I}_p^{(1)}}. \quad (66)$$

Given $\lambda_{n_1} < \lambda_{n_2}$, and exploiting that the density profile within the nudging region can be written as a linear combination of $e^{x/\lambda_{n_1}}$ and $e^{x/\lambda_{n_2}}$ (see Eq. (63) and boundary conditions), one finds $\rho'/\rho \sim \lambda_{n_2}^{-1}$ for $|x/\lambda_1| \gg 1$. The relative polarization in the nudging bulk is thus given by

$$\left(\frac{p}{\rho}\right)_n = \frac{D}{v(x)\lambda_{n_2}\mathcal{I}_p^{(1)}} - \frac{\mathcal{I}_p^{(1)}}{\mathcal{I}_p^{(1)}}. \quad (67)$$

For a nudging layer in the negative halfspace, one finds that $(p/\rho)_n$ is always less or equal to zero and becomes extremal for $\alpha = \pi/2$ as can be inferred from the upper panel of Fig. 8. Also, the higher the swimmer's activity, the greater the extremum in the bulk polarization. The lower panel of Fig. 8 displays a convincing agreement between the approximate theoretical prediction (67) and exact numerical solutions [106] up to Péclet numbers \mathcal{P} on the order of 50. The subsequent growing mismatch

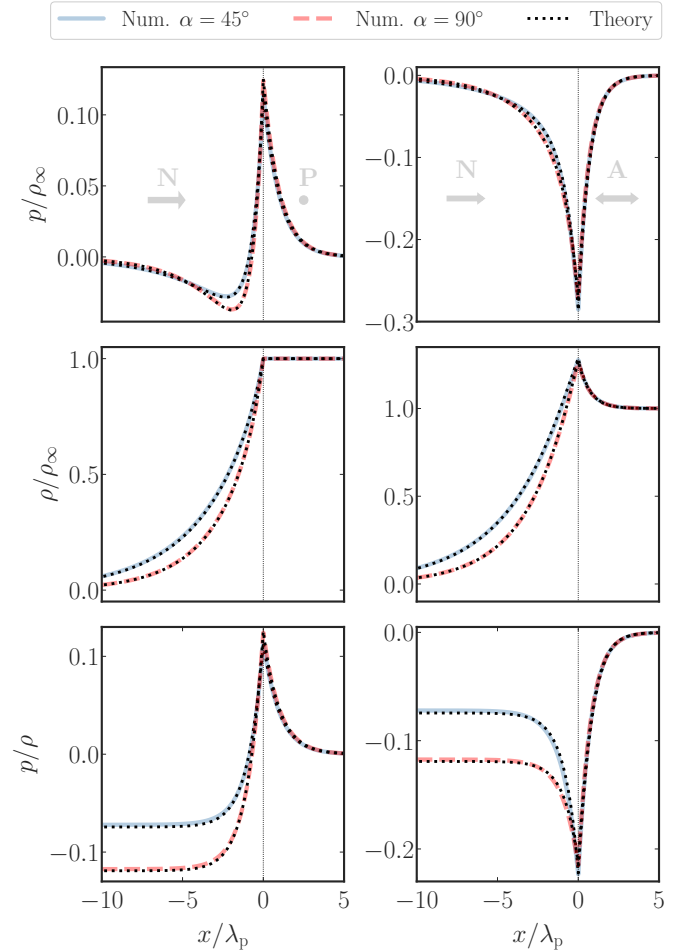


FIG. 7. Exact numerical solutions [106] for density and polarization profiles compared to theory for $\mathcal{P} = 1$. Lengths and velocities are measured in units of $\sqrt{D/D_r}$ and $\sqrt{2DD_r}$. Left panels correspond to a nudging-passive interface, while the right panels depict the situation at a nudging-active interface. Theoretical curves were obtained using Eq. (63), and the coefficients C_i are determined by the boundary and continuity conditions (64) and (65). All profiles are given relative to the bulk density ρ_∞ inside the active/passive bulk. The bottom panels depict the relative polarization.

between both originates in the fact that there exists no one-to-one mapping between the (approximate) analytic theory and the simple 2-state model in the case of a nudging interface (see Sec. IV A 2).

As explicitly checked in Sec. III C 1, but proven to hold generally [88], the total polarization $P_{\text{tot}} = \int_{-\infty}^{\infty} dx p(x)$ is determined by the difference of the respective bulk fluxes $v_i \rho_i$ divided by $2D_r$ [cf. Eq. (30)]. The bulk fluxes associated with the nudging and the passive region are both zero. The former vanishes because the bulk density $\rho_n = 0$, whereas, for the latter, $v = 0$. Thus, for a nudging-passive interface, $P_{\text{tot}} = 0$. Vanishing bulk fluxes therefore explain the change of sign in the polarization profile for the nudging-passive interface (see upper left panel of Fig. 7). For the nudging-active interface, one

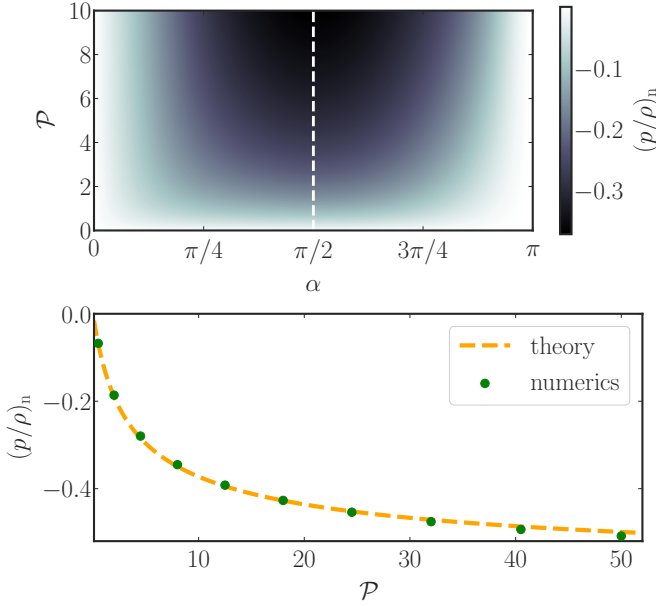


FIG. 8. Relative bulk polarization $(p/\rho)_n$ within the nudging region. Upper panel: Heat map of $(p/\rho)_n$ as function of the Péclet number \mathcal{P} and acceptance angle α according to Eq. (66). The vertical dashed line depicts the extremal curve (minimum) of $(p/\rho)_n$ with respect to α . Lower panel: The dashed curve corresponds to the (approximate) prediction (67), while the circles are obtained from exact numerical solutions [106]. Both were calculated at an acceptance angle $\alpha = \pi/2$.

finds $P_{\text{tot}} = -\rho_a v_a / (2D_r)$, which coincides with the total polarization of a passive-active interface [see Eq. (30)]. We verified these results for P_{tot} at the considered nudging interfaces analytically and numerically.

Since merely the total polarization is determined by bulk quantities, but not the local polarization profile $p(x)$ itself, a thorough discussion and physical interpretation of the respective polarization layers (active, passive, nudging) follows in the next section.

IV. DISCUSSION

A. The 2-species model

The emerging polarization and inhomogeneous density distribution in the vicinity of a sudden activity step are easily understood within a simple 2-species model [3, 65, 79, 92, 112]. In this onedimensional run-and-tumble model, a Janus swimmer is either oriented parallel or anti-parallel with respect to the x -axis. The orientation flips at a rate k according to an underlying dichotomous Markov process. Besides undergoing thermal diffusion, the particle propels actively with a position dependent swim speed $v_{\pm}(x)$, which might also depend on the orientation (\pm) of the particle in order to mimic the nudging. We define the probability densities $n_{\pm}(x, t)$

and $n_{\pm}(x, t)$ for encountering the particle at time t at position x , oriented parallel (+) or anti-parallel (−) with respect to the x -axis. The corresponding fluxes $J_{\pm}(x, t)$ contain contributions from both thermal agitation and from active propulsion, and are given by

$$J_+(x, t) = -Dn'_+(x, t) + v_+(x)n_+(x, t), \quad (68)$$

$$J_-(x, t) = -Dn'_-(x, t) + v_-(x)n_-(x, t). \quad (69)$$

We define the density $\rho \equiv n_+ + n_-$ and the polarization $p \equiv n_+ - n_-$. (Since this section is exclusively dedicated to the 2-species model, we use the same symbols as for the continuous-angle model.) After the system reaches its steady state, the total flux $J_+ + J_-$ vanishes and one finds the following balance condition

$$D\rho' = \frac{v_+ + v_-}{2}\rho + \frac{v_+ - v_-}{2}p. \quad (70)$$

The temporal evolution of the respective densities is given by

$$\begin{aligned} \dot{n}_+ &= -J'_+ - k(n_+ - n_-) \\ &= Dn''_+ - (v_+ n_+)' - k(n_+ - n_-), \end{aligned} \quad (71)$$

$$\begin{aligned} \dot{n}_- &= -J'_- + k(n_+ - n_-) \\ &= Dn''_- + (v_- n_-)' + k(n_+ - n_-). \end{aligned} \quad (72)$$

In the steady state ($\dot{n}_{\pm} = 0$), subtracting Eq. (72) from Eq. (71) yields

$$p'' = \frac{2k}{D}p + \left(\frac{v_+ - v_-}{2D}\rho + \frac{v_+ + v_-}{2D}p \right)'. \quad (73)$$

1. Fully Active/Passive:

The case of a symmetrically active/passive particle (regardless the orientation) is captured by setting $v_+ \equiv v = -v_-$. Equations (70) and (73) then reduce to

$$\rho' = \frac{v}{D}\rho, \quad p'' = \frac{p}{\lambda^2} + \frac{\rho}{D}v', \quad (74)$$

where we introduced the characteristic length scale

$$\lambda(x) \equiv \left[\frac{2k}{D} + \frac{v^2(x)}{D} \right]^{-1/2}. \quad (75)$$

The above equations for ρ , p , as well as the definition of λ are structurally equal to Eqs. (17), (18) and (19) for ρ , p and λ in the (approximate) model for continuous rotation. Upon the mapping $2k \rightarrow D_r$, $v \rightarrow v/\sqrt{2}$, $\rho \rightarrow \rho/\sqrt{2}$, the models become equivalent. One therefore applies the same methods as in section III C 1 to receive the analytical solutions for $p(x)$ and $\rho(x)$. Both these functions as well as the respective particle species densities $n_{\pm}(x) = [\rho(x) \pm p(x)]/2$ are plotted in the upper panel of Fig. 9. All the quantities are normalized by the bulk density $\rho_{\infty} = \rho(x \rightarrow \infty)$ within the passive region.

2. Nudging

Within the framework of the 2-species model, a nudging process is modelled by setting $v_+ \equiv v$ and $v_- \equiv 0$ for nudging to the right (or vice versa for left-nudging). The flux-balance condition (70) and Eq. (73) for the polarization then become

$$\rho' = \frac{v}{D} \frac{\rho}{2} + \frac{v}{D} \frac{p}{2}, \quad (76)$$

$$p'' = \frac{2k}{D} p + \frac{v}{D} \left(\frac{\rho'}{2} + \frac{p'}{2} \right) + \frac{v'}{D} \left(\frac{\rho}{2} + \frac{p}{2} \right). \quad (77)$$

These equations also have the same structure as their counterparts (54) and (55) for the continuous-rotation model. Thus, the methods used in section IIID can be applied in order to determine the polarization and density profiles. Note, however, that here, the 2-species and the continuous-angle model can not be mapped on each other. There exists no unique acceptance angle α to ensure $v/2 = v_0 \mathcal{I}_{(\rho,p)}^{(1,2)}$ for all coefficients $\mathcal{I}_{(\rho,p)}^{(1,2)}$ defined in (56)-(59), where v_0 denotes the Janus swimmer's propulsion speed in the continuous model. Nevertheless, at least qualitatively, polarization and density profiles in the 2-species model display the same features as their counterparts in the continuous model as can be inferred from the second and third panel of Fig. 9 (cf. Fig. 7). A more thorough discussion of the nudging process within the framework of the 2-state model, and a comparison to the continuous model can be found in App. B 2 and B 3.

B. Active-Passive interface

To gain an intuitive understanding of the emerging polarization layer at an active-passive interface, focus on the upper panel of Fig. 9. For the sake of brevity we denote particles pointing to the left and right by L and R , respectively. We first consider the situation on the active side, where the particle motion might be regarded as quasi-ballistic. While R -particles get stuck at the interface due to the ceasing propulsion, L -particles quickly “escape” the interfacial region. This sorting mechanism leads to a majority of R -particles at the interface caused by hidden bulk currents [88]. We now qualitatively explain the shape two polarization layers. In the passive region, the characteristic decay length $\lambda_p = \sqrt{D/(2k)}$ of the polarization is obtained by setting $v(x) = 0$ in Eq. (75). It is intuitively understood since the particle's motion on the passive side is ordinary diffusion characterized by diffusivity D . The spreading of the excess polarization into the passive region is limited by the characteristic time $2k$ of the dichotomous process that flips the particle orientation. Therefore, up to a prefactor, λ_p coincides with the mean-squared displacement of a passive particle. On the active side, a “sedimentation pressure” joins the game. Its cause is an “active swim force” ζv (with friction ζ) directed towards the interface

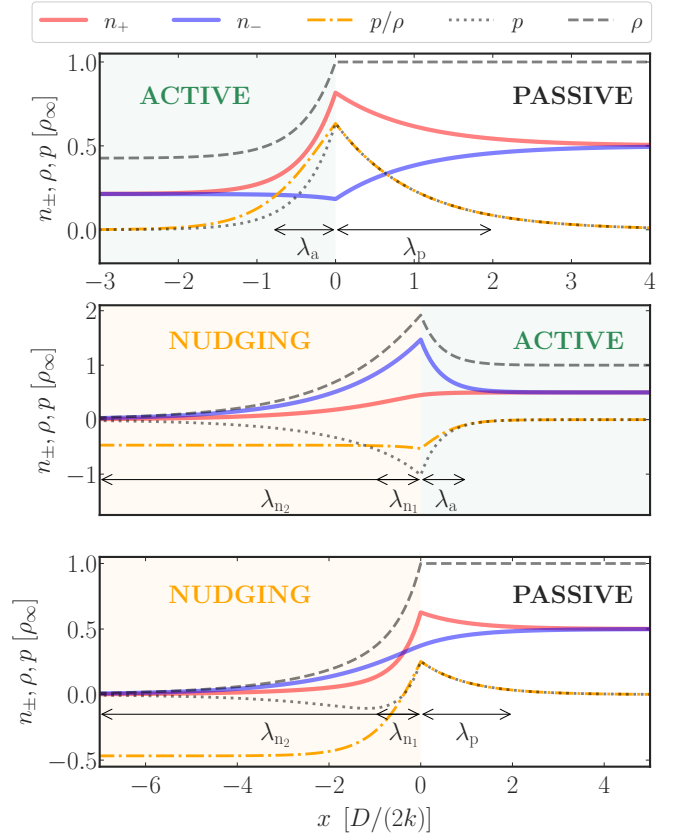


FIG. 9. 2-Species Model. Analytical polarization and density profiles, $p(x)$ and $\rho(x)$, the ratio p/ρ , as well as the corresponding species concentrations $n_{\pm}(x) = [\rho(x) \pm p(x)]/2$ of right- and left-oriented particles for an active-passive, nudging-active and nudging-passive interface at $x = 0$. All quantities are normalized by the respective constant bulk density $\rho_{\infty} = \rho(x \rightarrow \infty)$. Natural length scales of the polarization layers on the active and passive regions are denoted by λ_a and λ_p , respectively. The two length scales characterizing the nudging layer are labeled $\lambda_{n1,2}$.

for the R -particles and away from it for L -particles. One thus might regard R -particles as “heavy” and L -particles as “buoyant”. The sedimentation process therefore compresses the extension λ_a of the polarization layer according to Eq. (75) on the active side. Last but not least, for a highly persistent motion ($v^2/(2kD) \gg 1$), the polarization layer on the active side obeys the barometric formula $\exp(-v\zeta x/\zeta D)$, with the swim force instead of gravity and ζD for $k_B T$, according to the Sutherland-Einstein relation. In the same limit follows the motility-induced density suppression $\rho_a/\rho_p = \lambda_p/\lambda_a \propto v^{-1}$, which is a well-known result [3, 91] for run-and-tumble particles.

C. Nudging-Active interface

We now focus on the second panel of Fig. 9, which depicts $p(x)$, $\rho(x)$ and $n_{\pm}(x)$ in the vicinity of a nudging-

active interface. That is, while both particle species perform persistent motion within the active region, only the R -particles propel actively inside the nudging region. The R -species therefore does not display a sudden change (kink) in their density $n_+(x)$ upon crossing the interface, as they do not experience a sudden activity drop. In the active halfspace, R -particles quickly “escape” the interfacial area into the active region whereas L -particles get stuck at the interface and translate only diffusively into the nudging region. We thus observe an excess of L -particles at the interface, and therefore a negative polarization. The extent λ_a of the polarization layer on the active side is again determined by the interplay between Brownian motion and the “sedimentation process”, this time with “heavy” L - and “buoyant” R -particles. This symmetry between “heavy” and “buoyant” particle species is broken in the nudging region. There, R -particles are “heavy” and therefore nudged towards the interface whereas the L -species are passive Brownian particles. Close to the interface, the decay of density and polarization into the nudging region is therefore characterized by a length scale $\lambda_{n_1} \neq \lambda_a$. Referring back to the upper panel of Fig. 6, we infer that λ_{n_1} is still quite similar to the characteristic decay length λ_a pertaining to a purely active region. Notice that after a distance of λ_{n_1} the relative polarization p/ρ approaches a constant value given by Eq. (67). This is a distinctive feature of the nudging bulk, characterized by swim speed and acceptance angle of the nudging procedure. In contrast to a purely active or passive half space, both the polarization $p(x \rightarrow \infty)$ and the density $\rho(x \rightarrow \infty)$ of the nudging bulk approach zero since every particle is inevitably nudged towards the interface until it crosses it. The decay of the absolute polarization and density profiles towards zero is described by the second characteristic length scale $\lambda_{n_2} > \lambda_{n_1}$.

D. Nudging-Passive interface

Here we focus on the polarization and density profiles and the respective species concentrations presented in the last panel of Fig. 9. Now, only R -particles propel actively inside the nudging region, while both particle species behave like ordinary Brownian particles in the passive region. Therefore, the L -particles can cross the interface smoothly and their density $n_-(x)$ does not display a kink. We observe an excess of R -particles at the interface by virtue of the inherently biased nudging process, and thus a positive polarization. The extent λ_p of the polarization layer on the passive side is determined by the distance $\sqrt{D/(2k)}$ travelled by thermal diffusion during the characteristic time scale $2k$ of the orientation flipping process. The imbalance between the “heavy” R - and passive L -particles determines the spreading of the polarization into the nudging region. Due to the “removal” of R -particles towards the interface by virtue of the nudging procedure, the polarization even changes

sign and becomes negative over the characteristic length scale λ_{n_1} before it converges to zero over the length scale λ_{n_2} as discussed in the previous scenario. This distinctive shape of the polarization is a consequence of hidden bulk currents [88] as already discussed in Sec. III D.

V. CONCLUSION

In this article, we have studied properties of a single Janus-type swimmer in the vicinity of a motility step. Within an approximate ABP model, we derived analytical expressions for the polarization and density profiles of a Janus particle at planar activity steps. We showed that they agree well with exact numerical solutions [106] and experimental data (see our accompanying article [1]). Key features of polarization and density profiles at motility steps are discussed and show great similarities to those observed for MIPS [74]. As a consistency check, we also showed that the total polarization caused by the motility step is determined by the difference of (hidden) bulk fluxes [88], and thus constitutes a state function. We further showed that the bulk density ratio between two regions of distinct but constant activity is determined by the ratio of the respective effective diffusion coefficients independent of the shape of the activity profile that mediates between the two bulks. Motivated by the versatile experimental technique of photon nudging [95, 96], we then generalized our theoretical results to the situation of orientation-dependent propulsion speeds. We conclude that the co-localization of polarization and density patterns is a unique trait that distinguishes intrinsically active from passive matter at various interfaces.

ACKNOWLEDGEMENTS

We thank Paul Cervenak and Anton Stall for their contributions to the development of our theory in the course of their theses. We acknowledge funding by Deutsche Forschungsgemeinschaft (DFG) via SPP 1726/1 and KR 3381/6-1, and by Czech Science Foundation (project No. 20-02955J). Viktor Holubec gratefully acknowledges support by the Humboldt foundation.

REFERENCES

- [1] N. Söker, S. Auschra, V. Holubec, F. Cichos, and K. Kroy, “Activity fields,” (2020), to be published.
- [2] S. Ramaswamy, Annual Review of Condensed Matter Physics **1**, 323 (2010).
- [3] M. E. Cates, Reports on Progress in Physics **75** (2012).
- [4] P. Romanczuk, M. Bär, W. Ebeling, B. Lindner, and L. Schimansky-Geier, The European Physical Journal Special Topics **202**, 1–162 (2012).
- [5] C. Bechinger, R. Di Leonardo, H. Löwen, C. Reichhardt, G. Volpe, and G. Volpe, Reviews of Modern Physics **88**, 045006 (2016).

- [6] T. Vicsek and A. Zafeiris, *Physics Reports* **517**, 71–140 (2012).
- [7] S. Sponberg, *Physics Today* **70**, 34–40 (2017).
- [8] H. Berg, *E. coli in motion* (Springer, New York, 2004).
- [9] H.-R. Jiang, N. Yoshinaga, and M. Sano, *Physical Review Letters* **105**, 268302 (2010).
- [10] G. Falasco, R. Pfaller, A. Bregulla, F. Cichos, and K. Kroy, *Physical Review E - Statistical, Nonlinear, and Soft Matter Physics* **94** (2016).
- [11] I. Buttinoni, G. Volpe, F. Kümmel, G. Volpe, and C. Bechinger, *Journal of Physics Condensed Matter* (2012).
- [12] M. Yang and M. Ripoll, *Soft Matter* **9**, 4661 (2013).
- [13] J. L. Moran, P. M. Wheat, and J. D. Posner, *Physical Review E* **81** (2010).
- [14] R. Golestanian, T. B. Liverpool, and A. Ajdari, *Physical Review Letters* **94** (2005).
- [15] J. R. Howse, R. A. Jones, A. J. Ryan, T. Gough, R. Vafabakhsh, and R. Golestanian, *Physical Review Letters* **99**, 8 (2007).
- [16] T. Bickel, A. Majee, and A. Würger, *Physical Review E - Statistical, Nonlinear, and Soft Matter Physics* **88** (2013).
- [17] M. N. Popescu, S. Dietrich, M. Tasinkevych, and J. Ralston, *European Physical Journal E* **31**, 351 (2010).
- [18] N. Sharifi-Mood, A. Mozaffari, and U. M. Córdoba-Figueroa, *Journal of Fluid Mechanics* **798**, 910–954 (2016).
- [19] S. Saha, S. Ramaswamy, and R. Golestanian, *New Journal of Physics* **21**, 063006 (2019).
- [20] B. Nasouri and R. Golestanian, “Non-equilibrium interaction of phoretically active janus particles: a generic approach,” (2020), arXiv:2005.09429 [cond-mat.soft].
- [21] Z. Shen, A. Würger, and J. S. Lintuvuori, *The European Physical Journal E* **41** (2018).
- [22] P. Bayati, M. N. Popescu, W. E. Usual, S. Dietrich, and A. Najafi, *Soft Matter* **15**, 5644–5672 (2019).
- [23] T. Bickel, G. Zecua, and A. Würger, *Physical Review E - Statistical, Nonlinear, and Soft Matter Physics* **89**, 1 (2014).
- [24] A. Geiseler, P. Hänggi, and F. Marchesoni, *Scientific Reports* **7**, 1 (2017).
- [25] A. Geiseler, P. Hänggi, and F. Marchesoni, *Entropy* **19**, 1 (2017).
- [26] A. Geiseler, P. Hänggi, F. Marchesoni, C. Mulhern, and S. Savel’ev, *Physical Review E* **94** (2016).
- [27] J. D. Olarte-Plata and F. Bresme, *The Journal of Chemical Physics* **152**, 204902 (2020).
- [28] S. Steffenoni, K. Kroy, and G. Falasco, *Physical Review E* **94**, 1 (2016).
- [29] S. Steffenoni, G. Falasco, and K. Kroy, *Physical Review E* **95**, 1 (2017).
- [30] S. C. Takatori and J. F. Brady, *Soft Matter* **11**, 7920–7931 (2015).
- [31] A. P. Solon, M. E. Cates, and J. Tailleur, *The European Physical Journal Special Topics* **224**, 1231–1262 (2015).
- [32] J. Bialké, H. Löwen, and T. Speck, *EPL (Europhysics Letters)* **103**, 30008 (2013).
- [33] F. S. Gnesotto, F. Mura, J. Gladrow, and C. P. Broedersz, *Reports on Progress in Physics* **81**, 066601 (2018).
- [34] U. Basu, C. Maes, and K. Netočný, *Physical Review Letters* **114** (2015).
- [35] J. Elgeti and G. Gompper, *EPL (Europhysics Letters)* **101**, 48003 (2013).
- [36] T. Speck and R. L. Jack, *Physical Review E* **93** (2016).
- [37] C. G. Wagner, M. F. Hagan, and A. Baskaran, *Journal of Statistical Mechanics: Theory and Experiment* **2017**, 043203 (2017).
- [38] U. Seifert, *Reports on Progress in Physics* **75**, 126001 (2012).
- [39] A. Ryabov, V. Holubec, M. H. Yaghoubi, M. Varga, M. E. Foulaadvand, and P. Chvosta, *Journal of Statistical Mechanics: Theory and Experiment* **2016**, 093202 (2016).
- [40] V. Holubec, A. Ryabov, M. Yaghoubi, M. Varga, A. Khodaei, M. Foulaadvand, and P. Chvosta, *Entropy* **19**, 119 (2017).
- [41] J. Rodenburg, M. Dijkstra, and R. van Roij, *Soft Matter* **13**, 8957–8963 (2017).
- [42] J. Rodenburg, S. Paliwal, M. de Jager, P. G. Bolhuis, M. Dijkstra, and R. van Roij, *The Journal of Chemical Physics* **149**, 174910 (2018).
- [43] A. P. Solon, J. Stenhammar, M. E. Cates, Y. Kafri, and J. Tailleur, *Physical Review E* **97**, 1 (2018).
- [44] A. P. Solon, J. Stenhammar, M. E. Cates, Y. Kafri, and J. Tailleur, *New Journal of Physics* **20**, 075001 (2018).
- [45] T. F. F. Farage, P. Krinninger, and J. M. Brader, *Physical Review E* **91** (2015).
- [46] A. Sharma and J. M. Brader, *Physical Review E* **96** (2017).
- [47] M. J. Lighthill, *Communications on Pure and Applied Mathematics* **5**, 109–118 (1952).
- [48] E. Lauga and T. R. Powers, *Reports on Progress in Physics* **72** (2009).
- [49] J.-P. Hansen and I. R. McDonald, *Theory of simple liquids : with applications to soft matter* (Academic Press, Amsterdam Boston, 2013).
- [50] C. Ganguly and D. Chaudhuri, *Physical Review E* **88** (2013).
- [51] D. Chaudhuri, *Physical Review E* **90** (2014).
- [52] E. Fodor, C. Nardini, M. E. Cates, J. Tailleur, P. Visco, and F. van Wijland, *Physical Review Letters* **117** (2016).
- [53] C. Nardini, E. Fodor, E. Tjhung, F. van Wijland, J. Tailleur, and M. E. Cates, *Physical Review X* **7** (2017).
- [54] D. Mandal, K. Klymko, and M. R. DeWeese, *Physical Review Letters* **119** (2017).
- [55] U. M. B. Marconi, A. Puglisi, and C. Maggi, *Scientific Reports* **7** (2017).
- [56] P. Pietzonka and U. Seifert, *Journal of Physics A: Mathematical and Theoretical* **51**, 01LT01 (2017).
- [57] S. Shankar and M. C. Marchetti, *Physical Review E* **98** (2018).
- [58] T. Speck, *EPL (Europhysics Letters)* **123**, 20007 (2018).
- [59] U. Khadka, V. Holubec, H. Yang, and F. Cichos, *Nature Communications* **9**, 1 (2018).
- [60] L. Caprini, U. M. B. Marconi, A. Puglisi, and A. Vulpiani, *Journal of Statistical Mechanics: Theory and Experiment* **2019**, 053203 (2019).
- [61] L. Dabelow, S. Bo, and R. Eichhorn, *Physical Review X* **9** (2019).
- [62] G. Szamel, *Physical Review E* **100** (2019).
- [63] V. Holubec, S. Steffenoni, G. Falasco, and K. Kroy, “Active brownian heat engines,” (2020), arXiv:2001.10448 [cond-mat.stat-mech].
- [64] E. Flenner and G. Szamel, “Active matter: quantifying the departure from equilibrium,” (2020),

- arXiv:2004.11925 [cond-mat.soft].
- [65] N. Razin, “The entropy production of an active particle in a box,” (2020), arXiv:2008.08088 [cond-mat.stat-mech].
- [66] J. Schnakenberg, *Reviews of Modern Physics* **48**, 571–585 (1976).
- [67] P. Gaspard, *The Journal of Chemical Physics* **120**, 8898–8905 (2004).
- [68] P. Gaspard, *Journal of Statistical Physics* **117**, 599–615 (2004).
- [69] B. Andrae, J. Cremer, T. Reichenbach, and E. Frey, *Physical Review Letters* **104** (2010).
- [70] J. Li, J. M. Horowitz, T. R. Gingrich, and N. Fakhri, *Nature Communications* **10** (2019).
- [71] D. M. Busiello and A. Maritan, *Journal of Statistical Mechanics: Theory and Experiment* **2019**, 104013 (2019).
- [72] E. Roldán and J. M. R. Parrondo, *Physical Review Letters* **105** (2010).
- [73] O. Lieleg, M. M. A. E. Claessens, C. Heussinger, E. Frey, and A. R. Bausch, *Physical Review Letters* **99** (2007).
- [74] M. E. Cates and J. Tailleur, *Annual Review of Condensed Matter Physics* **6**, 219–244 (2015).
- [75] M. E. Cates and J. Tailleur, *Epl* **101** (2013).
- [76] S. Paliwal, J. Rodenburg, R. van Roij, and M. Dijkstra, *New Journal of Physics* **20**, 015003 (2018).
- [77] S. Hermann, P. Krinninger, D. de las Heras, and M. Schmidt, *Physical Review E* **100** (2019).
- [78] A. Patch, D. M. Sussman, D. Yllanes, and M. C. Marchetti, *Soft Matter* **14**, 7435–7445 (2018).
- [79] J. Tailleur and M. E. Cates, *Physical Review Letters* **100**, 218103 (2008).
- [80] D. Richard, H. Löwen, and T. Speck, *Soft Matter* **12**, 5257–5264 (2016).
- [81] K. Shida and T. Kawai, *Physica A: Statistical Mechanics and its Applications* **162**, 145–160 (1989).
- [82] S. McNamara and W. R. Young, *Physics of Fluids A: Fluid Dynamics* **4**, 496–504 (1992).
- [83] M. E. Cates and J. Tailleur, *EPL (Europhysics Letters)* **101**, 20010 (2013).
- [84] S. Hermann and M. Schmidt, *Soft Matter* **14**, 1614–1621 (2018).
- [85] J. Vachier and M. G. Mazza, *The European Physical Journal E* **42** (2019).
- [86] M. Enculescu and H. Stark, *Physical Review Letters* **107** (2011).
- [87] F. Ginot, A. Solon, Y. Kafri, C. Ybert, J. Tailleur, and C. Cottin-Bizonne, *New Journal of Physics* **20**, 115001 (2018).
- [88] S. Hermann and M. Schmidt, *Physical Review Research* **2** (2020).
- [89] V. Prymidis, S. Paliwal, M. Dijkstra, and L. Filion, *The Journal of Chemical Physics* **145**, 124904 (2016).
- [90] S. Paliwal, V. Prymidis, L. Filion, and M. Dijkstra, *The Journal of Chemical Physics* **147**, 084902 (2017).
- [91] M. J. Schnitzer, *Physical Review E* **48**, 2553 (1993).
- [92] K. Malakar, V. Jemseena, A. Kundu, K. Vijay Kumar, S. Sabhapandit, S. N. Majumdar, S. Redner, and A. Dhar, *Journal of Statistical Mechanics: Theory and Experiment* **2018**, 043215 (2018).
- [93] A. Fischer, F. Schmid, and T. Speck, *Physical Review E* **101** (2020).
- [94] A. P. Bregulla, H. Yang, and F. Cichos, *ACS Nano* **8**, 6542 (2014).
- [95] M. Selmke, U. Khadka, A. P. Bregulla, F. Cichos, and H. Yang, *Physical Chemistry Chemical Physics* **20**, 10502 (2018).
- [96] M. Selmke, U. Khadka, A. P. Bregulla, F. Cichos, and H. Yang, *Physical Chemistry Chemical Physics* **20**, 10521 (2018).
- [97] G. Gompper, C. Bechinger, S. Herminghaus, R. Isele-Holder, U. B. Kaupp, H. Löwen, H. Stark, and R. G. Winkler, *European Physical Journal: Special Topics* **225**, 2061 (2016).
- [98] B. Qian, D. Montiel, A. Bregulla, F. Cichos, and H. Yang, *Chemical Science* **4** (2013).
- [99] G. Falasco and K. Kroy, *Physical Review E* **93**, 1 (2016).
- [100] K. Kroy and F. Cichos, *Hot brownian motion in Diffusive Spreading in Nature, Technology and Society* (Springer International Publishing, 2017).
- [101] E. Bertin, M. Droz, and G. Grégoire, *Physical Review E* **74** (2006).
- [102] R. Golestanian, *Physical Review Letters* **108** (2012).
- [103] M. E. Cates, *Reports on progress in physics. Physical Society (Great Britain)* **75**, 042601 (2012).
- [104] H. Risken, *The Fokker-Planck Equation – Methods of Solution and Applications*, 2nd ed., edited by H. Haken (Springer-Verlag Berlin Heidelberg, 1989).
- [105] C. W. Gardiner, *Handbook of Stochastic Methods for Physics, Chemistry and the Natural Sciences*, 2nd ed., edited by H. Haken (Springer-Verlag Berlin Heidelberg New York, 1985).
- [106] V. Holubec, K. Kroy, and S. Steffenoni, *Phys. Rev. E* **99**, 032117 (2019).
- [107] J. Tailleur and M. E. Cates, *Epl* **86** (2009).
- [108] A. J. Rodenburg, *Thermodynamic Variables for Active Brownian Particles : Pressure, Surface Tension, and Chemical Potential*, Ph.D. thesis, Utrecht University (2020).
- [109] M. B. Miller and B. L. Bassler, *Annual Review of Microbiology* **55**, 165–199 (2001).
- [110] A. P. Solon, J. Stenhammar, R. Wittkowski, M. Kardar, Y. Kafri, M. E. Cates, and J. Tailleur, *Physical Review Letters* **114**, 1 (2015).
- [111] M. J. Schnitzer, *Physical Review E* **48**, 2553 (1993).
- [112] G. H. Weiss, *Physica A: Statistical Mechanics and its Applications* **311**, 381–410 (2002).

Appendix A: Planar Activity Step

1. Density ratio and total polarization

a. Density ratio: Introducing the auxiliary quantities $\beta_{A,a} \equiv p_{\max} v_{A,a} \lambda_{A,a} / [D\rho(0)]$, Eqs. (26) and (27) evaluated at $x = 0$ and $x \rightarrow \infty$, respectively, yield

$$\rho(0) - \rho_A = \rho(0)\beta_A \quad (\text{A1})$$

$$\rho_a - \rho_A = \rho(0)(\beta_a + \beta_A). \quad (\text{A2})$$

Using these equations, density ratio can be expressed as $\rho_a/\rho_A = (1 + \beta_a)/(1 - \beta_a)$. Further using

$$\lambda_{A,a} = \left(\frac{D_r}{D} + \frac{v_{A,a}^2}{2D^2} \right)^{-1/2}, \quad (\text{A3})$$

$$\frac{p_{\max}}{\rho(0)} = \frac{v_A - v_a}{2D} \frac{\lambda_A \lambda_a}{\lambda_A + \lambda_a}, \quad (\text{A4})$$

from Eq. (28), implies $\rho_a/\rho_A = \lambda_a/\lambda_A$, as given in Eq. (29).

b. Total Polarization: From Eq. (30), we know that the total polarization P_{tot} is given by $p_{\max}(\lambda_A + \lambda_a)$. The coefficient p_{\max} can be expressed as $D(\rho_a - \rho_A)/(v_A \lambda_A - v_a \lambda_a)$ by virtue of Eq. (A2). Hence, the total polarization reads

$$P_{\text{tot}} = D(\rho_a - \rho_A) \frac{\lambda_a + \lambda_A}{v_A \lambda_A - v_a \lambda_a}. \quad (\text{A5})$$

Using $\rho_a/\rho_A = \lambda_a/\lambda_A$, we find that

$$P_{\text{tot}} = D \frac{(\rho_a - \rho_A)(\rho_a + \rho_A)}{v_A \rho_A + v_a \rho_a} \quad (\text{A6})$$

$$= D \frac{\rho_a^2 - \rho_A^2}{v_a^2 \rho_a^2 - v_A^2 \rho_A^2} (v_a \rho_a - v_A \rho_A). \quad (\text{A7})$$

Using the formula $\rho_a/\rho_A = \lambda_a/\lambda_A$ and the definition (A3) of $\lambda_{A,a}$, the factor in front of the term in parentheses turns out to be equal to $-1/(2D_r)$. One thus obtains $P_{\text{tot}} = (v_A \rho_A - v_a \rho_a)/(2D_r)$, as stated in Eq. (30).

2. Vanishing integral

The main result (41) for the density ratio reads

$$\frac{\rho(x)}{\rho(x_0)} = \sqrt{\frac{D_{\text{eff}}(x_0)}{D_{\text{eff}}(x)}} \exp \{ \mathcal{U}[v](x_0, x) \}, \quad (\text{A8})$$

with the emerging functional \mathcal{U} defined in Eq.(42). We will first prove that for the ratio of bulk densities, $\mathcal{U} \equiv 0$, within the framework of the 2-state model (see Sec. IV A). After that, we will describe how this proof generalizes to the continuous model.

First, we consider an arbitrary activity profile $v(x)$ whose inhomogenities are localized around a finite region beyond which the velocity assumes a single constant value, see Fig. 10 a). We will refer to the corresponding constant bulk densities as ρ_i , $i = 1, 2$. In the bulks, the polarization vanishes and thus the concentrations $n_{\pm}^{(i)}$ of the individual species equal, $n_{\pm}^{(i)} = \rho_i/2$. The corresponding fluxes between the two bulk regions can be expressed as

$$J_{12} = \frac{\rho_1}{2} (\nu_{12}^+ + \nu_{12}^-), \quad (\text{A9})$$

$$J_{21} = \frac{\rho_2}{2} (\nu_{21}^+ + \nu_{21}^-), \quad (\text{A10})$$

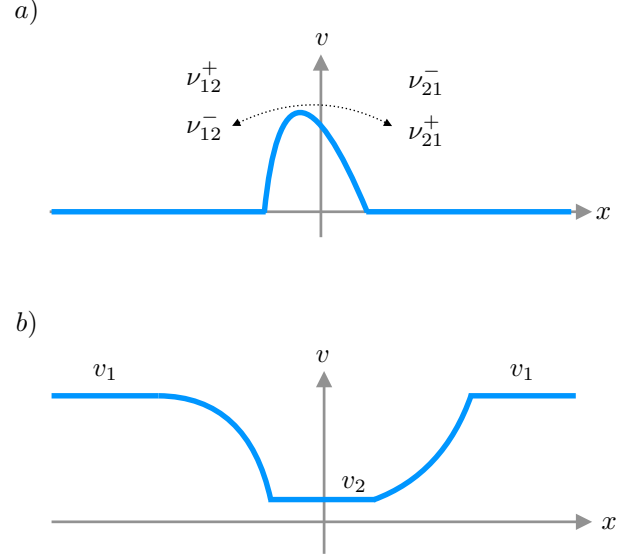


FIG. 10. Activity profiles $v(x)$ considered to prove that the integral \mathcal{U} vanishes. In the upper plot, ν_{ij}^{\pm} denote the transition rates of particles species (\pm) from the left to the right bulk region and vice versa. In the lower plot, $v_{1,2}$ denote the constant activities in the middle and the outer regions, respectively.

where we introduced the transition rates ν_{ij}^{\pm} of particle species (\pm) between the bulk region i and j . In the steady state, the (anti-)symmetry between the two particle species implies $\nu_{12}^+ = \nu_{21}^-$ and $\nu_{12}^- = \nu_{21}^+$. Flux balance $J_{12} = J_{21}$ then induces $\rho_1 = \rho_2$. For an arbitrary activity profile $v(x)$ with bulk activities given by a single constant, Eq. (A8) thus implies that $1 = \rho_1/\rho_2 = e^{\mathcal{U}}$ and hence $\mathcal{U} = 0$.

Now, we consider activity profiles of the form sketched in Fig. 10 b). Two bulk region with constant activity v_1 are interconnected by two arbitrary activity steps and an intermediate bulk region with a constant activity $v_2 \neq v_1$. From the first part of the proof, we know that $\rho_1/\rho_3 = 1$ as the activity in both regions is equal and constant. We thus know that $0 = \mathcal{U}[v_1, v_2] = \mathcal{U}_1[v_1] + \mathcal{U}_2[v_2]$, where we introduced the integrals $\mathcal{U}_{1,2}$ pertaining to the two activity profiles $v_{1,2}$. Since the total integral has to vanish for any intermediate set of activity gradients, both \mathcal{U}_1 and \mathcal{U}_2 must be zero. Therefore, for the 2-state model, $\rho_1/\rho_2 = \sqrt{D_{\text{eff}}(x_2)/D_{\text{eff}}(x_1)}$ for any activity profile that mediates between two bulk positions x_1 and x_2 .

To generalize this proof to the model with continuous orientation, it is enough to realize that for each orientation where the particle points to the right there exists an “anti” particle with orientation pointing to the left. These two particle orientation can be considered as the two species above, and, to finish the proof, it is thus enough to apply the above procedure to the whole (infinite) set of these orientation pairs.

3. Finite system – determine coefficients

region, respectively, read

$$p_a(x) = C_a \sinh\left(\frac{x}{\lambda_a}\right), \quad \lambda_a = \left(\frac{D_r}{D} + \frac{v_0^2}{2D^2}\right)^{-1/2} \quad (\text{A11})$$

$$p_p(x) = C_p \sinh\left(\frac{L-x}{\lambda_p}\right), \quad \lambda_p = \sqrt{\frac{D}{D_r}}, \quad (\text{A12})$$

$$\rho_a(x) = \rho_a(0) + \frac{C_a \lambda_a v_0}{D} \left[\cosh\left(\frac{x}{\lambda_a}\right) - 1 \right] \quad (\text{A13})$$

$$\rho_p(x) = \rho_a(x_a) = \text{const.} \quad (\text{A14})$$

The emerging integration constants C_a and C_p are fixed by the continuity conditions

$$p_a(x_a) = p_p(x_a), \quad (\text{A15})$$

$$p_a'(x_a) - p_p'(x_a) = \frac{v_0}{2D} \rho(x_a), \quad (\text{A16})$$

which follow from Eq. (16). The first one allows us to express one integration constant in terms of the other:

$$C_p = C_a \frac{\sinh[x_a/\lambda_a]}{\sinh[(L-x_a)/\lambda_p]}. \quad (\text{A17})$$

The general solutions (44) and (45) to the particle's density distribution $\rho_{a/p}(x)$ and polarization $p_{a/p}(x)$ within the active ($0 \leq x \leq x_a$) and passive ($a < x \leq L$)

Before we employ the condition (A16), we exploit the normalization condition $\int_{-L}^L dx \rho(x) = 1$, to calculate the density at the interface $\rho(x_a)$. Respecting the symmetry of the considered problem, we get

$$\begin{aligned} \frac{1}{2} &= \int_0^L dx \rho(x) = \int_0^{x_a} dx \rho_a(x) + \int_{x_a}^L dx \rho_p(x) \\ &= \int_0^{x_a} dx \rho_a(x) + (L-x_a) \rho_a(x_a) \\ &= x_a \rho_a(0) + \frac{C_a \lambda_a v_0}{D} \left[\lambda_a \sinh\left(\frac{x_a}{\lambda_a}\right) - x_a \right] + (L-x_a) \left\{ \rho_a(0) + \frac{C_a \lambda_a v_0}{D} \left[\cosh\left(\frac{x_a}{\lambda_a}\right) - 1 \right] \right\}. \end{aligned} \quad (\text{A18})$$

Solving this equation for $\rho_a(0)$, we find

$$\rho_a(0) = \frac{1}{2L} - \left(1 - \frac{x_a}{L}\right) \frac{C_a \lambda_a v_0}{D} \left[\cosh\left(\frac{x_a}{\lambda_a}\right) - 1 \right] - \frac{x_a}{L} \frac{C_a \lambda_a v_0}{D} \left[\frac{\lambda_a}{x_a} \sinh\left(\frac{x_a}{\lambda_a}\right) - 1 \right]. \quad (\text{A19})$$

Substituting this relation into Eq. (A13) yields

$$\rho_a(x_a) = \frac{1}{2L} + \frac{x_a}{L} \frac{C_a \lambda_a v_0}{D} \left[\cosh\left(\frac{x_a}{\lambda_a}\right) - \frac{\lambda_a}{x_a} \sinh\left(\frac{x_a}{\lambda_a}\right) \right]. \quad (\text{A20})$$

Finally, plugging this result into Eq. (A16) and using Eq. (A17) for C_p renders a linear equation for C_a , which is straightforwardly solved. With the definitions (52)-(53),

$$P_{\max} \equiv \frac{v_0}{2D} \frac{\lambda_a \lambda_p}{\lambda_a + \lambda_p}, \quad r_\rho \equiv \frac{\lambda_a}{\lambda_p}, \quad (\text{A21})$$

one finds that

$$C_a = \frac{1}{2L \sinh(x_a/\lambda_a)} \frac{P_{\max}}{\coth\left(\frac{x_a}{\lambda_a}\right) - \frac{1-r_\rho}{L} \left[x_a \coth\left(\frac{L-x_a}{\lambda_p}\right) - \lambda_a\right]}. \quad (\text{A22})$$

The approximation $\coth(x_a/\lambda_a) \approx \coth((L-x_a)/\lambda_p) \approx 1$ in the above equations then leads to the polarization and density profiles (48)-(51) given in the main text.

Appendix B: Nudging Layer

1. Continuous model

As derived in Sec. IIID, within a nudging region, the vector $\mathbf{X}(x) = [p'(x), p(x), \rho(x)]^\top$ composed of the polarization profile $p(x)$, its derivative, and the density $\rho(x)$ obeys an equation of the form $\mathbf{X}' = \mathbf{\Lambda}\mathbf{X}$. In contrast to the discussion in the main text we now resort to a dimensionless description by introducing $\lambda_p = \sqrt{D/D_r}$ as natural unit of length. The matrix $\mathbf{\Lambda}$ can then be expressed in terms of a single parameter – the Péclet number $\mathcal{P} = v_0^2/(2DD_r)$ – and reads

$$\mathbf{\Lambda} = \begin{pmatrix} \sqrt{2\mathcal{P}}\mathcal{I}_p^{(2)} & 1 + 2\mathcal{P}\mathcal{I}_\rho^{(2)}\mathcal{I}_p^{(1)} & 2\mathcal{P}\mathcal{I}_\rho^{(1)}\mathcal{I}_\rho^{(2)} \\ 1 & 0 & 0 \\ 0 & \sqrt{2\mathcal{P}}\mathcal{I}_p^{(1)} & \sqrt{2\mathcal{P}}\mathcal{I}_\rho^{(1)} \end{pmatrix} \quad (\text{B1})$$

The quantities $\mathcal{I}_{\rho,p}^{(1,2)}$, defined in Eqs. (56)-(59), characterize the influence of the restricted acceptance angle α on the heating laser. Clearly, the eigenvalues $\lambda_{n_i}^{-1}$ of the matrix $\mathbf{\Lambda}$ determine the general solution $\mathbf{X}(x)$. The characteristic equation $|\mathbf{\Lambda} - \lambda^{-1}\mathbf{1}| = 0$ renders the cubic equation $\lambda^{-3} + a\lambda^{-2} + b\lambda^{-1} + c = 0$, with

$$a \equiv -(\mathcal{I}_\rho^{(1)} + \mathcal{I}_p^{(2)})\sqrt{2\mathcal{P}}, \quad (\text{B2})$$

$$b \equiv 2\left(\mathcal{I}_\rho^{(1)}\mathcal{I}_p^{(2)} - 2\left[\mathcal{I}_\rho^{(2)}\right]^2\right)\mathcal{P} - 1, \quad (\text{B3})$$

$$c \equiv \mathcal{I}_\rho^{(1)}\sqrt{2\mathcal{P}}. \quad (\text{B4})$$

Using the Tschirnhaus-Vieta approach to the solution of cubic equations, one finds that all three roots are real-valued and can be written in the form

$$\lambda_{n_1}^{-1} = -\frac{a}{3} + 2\sqrt{-q}\cos\left(\frac{\gamma}{3}\right), \quad (\text{B5})$$

$$\lambda_{n_2}^{-1} = -\frac{a}{3} + 2\sqrt{-q}\cos\left(\frac{\gamma}{3} + \frac{4\pi}{3}\right), \quad (\text{B6})$$

$$\lambda_{n_3}^{-1} = -\frac{a}{3} + 2\sqrt{-q}\cos\left(\frac{\gamma}{3} + \frac{2\pi}{3}\right), \quad (\text{B7})$$

where we introduced the auxiliary quantities

$$q \equiv \frac{3b - a^2}{9}, \quad (\text{B8})$$

$$r \equiv \frac{9ab - 27c - 2a^3}{54}, \quad (\text{B9})$$

$$\gamma \equiv \arccos\left(\frac{r}{\sqrt{-q}}\right). \quad (\text{B10})$$

The dependence of the eigenvalues $\lambda_{n_i}^{-1}$ on the particle's propulsion speed (or Péclet number) and the acceptance angle α are graphically discussed in Sec. IIID of the main text as the analytical expressions above lack an immediate physical insight.

2. 2-Species Model

As derived in Sec. IVA, the governing equations for the polarization and density profiles within the framework of the 2-state model are structurally equivalent to those of the previously discussed continuous-angle model, namely $\mathbf{X} = \mathbf{\Lambda}_2\mathbf{X}$. In a dimensionless description (lengths expressed in units of $\sqrt{D/(2k)}$) the matrix $\mathbf{\Lambda}_2$ reads

$$\mathbf{\Lambda}_2 = \begin{pmatrix} \frac{\sqrt{\mathcal{P}_2}}{2} & 1 + \frac{\mathcal{P}_2}{4} & \frac{\mathcal{P}_2}{4} \\ 1 & 0 & 0 \\ 0 & \frac{\sqrt{\mathcal{P}_2}}{2} & \frac{\sqrt{\mathcal{P}_2}}{2} \end{pmatrix}, \quad (\text{B11})$$

where we introduced the Péclet number $\mathcal{P}_2 \equiv v^2/(2kD)$ pertaining to the 2-species model. The characteristic polynomial $|\mathbf{\Lambda}_2 - \lambda^{-1}\mathbf{1}| = 0$ delivers the cubic equation $\lambda^{-3} + a\lambda^{-2} + b\lambda^{-1} + c = 0$, with

$$a \equiv -\sqrt{\mathcal{P}_2}, \quad b \equiv -1, \quad c \equiv \sqrt{\mathcal{P}_2}/2. \quad (\text{B12})$$

The solutions are obtained using the same method as in the previous section (Tschirnhaus-Vieta approach).

3. Comparison

The upper panels of Fig. 11 compare the eigenvalues $\lambda_{n_i}^{-1}$ pertaining to the continuous model [a]) to those corresponding to the 2-state model [b)]. We infer that, within the plotting range, the eigenvalues of both models display the same qualitative behavior. This observation

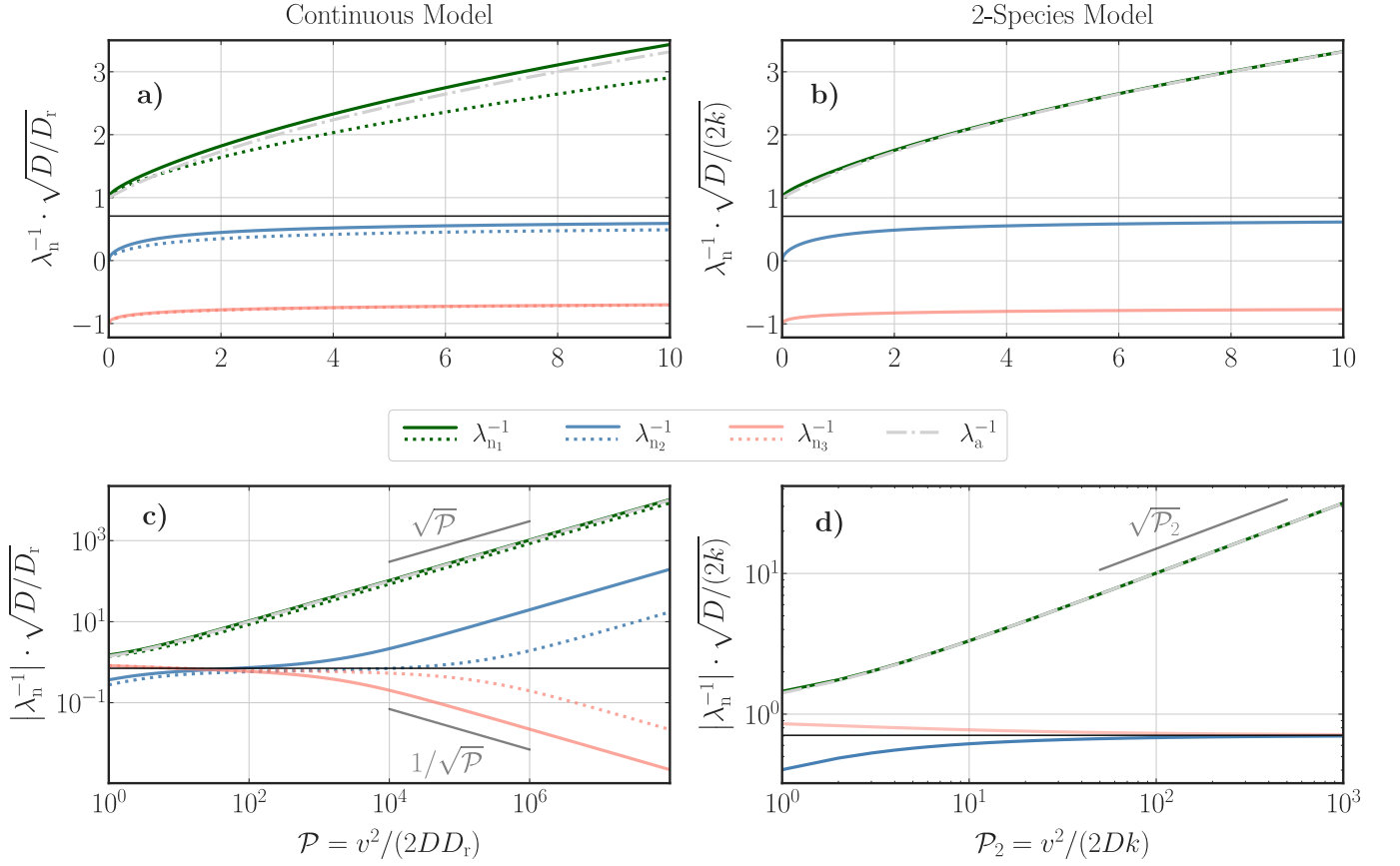


FIG. 11. Comparison of eigenvalues. *Left panels:* In **a**), Eigenvalues $\lambda_{n_i}^{-1}$ pertaining to the continuous-angle model are plotted against the Péclet number \mathcal{P} using equations (B5)-(B7) for two fixed acceptance angles, $\alpha = 45^\circ$ (dotted curves) and $\alpha = 90^\circ$ (solid curves). The dashed gray curve corresponds to the inverse length scale (or eigenvalue) $\lambda_a^{-1} = \sqrt{1 + \mathcal{P}}$ of a symmetrically active polarization layer. In **c**), the absolute value of eigenvalues $\lambda_{n_i}^{-1}$ are presented on a double-logarithmic scale. *Right panels:* The same eigenvalues pertaining to the 2-species model (cf. Sec. IV A) are plotted against the corresponding Péclet number \mathcal{P}_2 on a linear-linear [**b**] and a double logarithmic scale [**d**]. The gray dashed curve corresponds to $\lambda_a^{-1} = \sqrt{1 + \mathcal{P}_2}$, the (inverse) natural size of a fully active polarization layer. The dashed black horizontal lines in all four panels correspond to the value $1/\sqrt{2}$.

proves the intuitive conjunction that the 2-species model can serve as a simple model to explain the physics underlying the polarization and accumulation effects. There are, nevertheless, quantitative and qualitative differences between the two models. This becomes obvious from the lower panels of Fig. 11, where we plotted the absolute value of the eigenvalues $\lambda_{n_i}^{-1}$ of both models on a double-logarithmic scale to visualize their behavior for large Péclet numbers. We will qualitatively compare both models in the following. Besides Fig. 11, we will refer to the content of Tab. I showing the limiting behavior of all eigenvalues for low Péclet numbers. During the following discussion we will use the notion $\mathcal{P}_{(2)}$ in order to refer to both Péclet numbers \mathcal{P} and \mathcal{P}_2 . First, we focus our attention to the eigenvalue $\lambda_{n_1}^{-1}$, which, for low Péclet numbers, increases proportionally to $\sqrt{\mathcal{P}_{(2)}}$ irrespective of the underlying model. The (inverse) characteristic size λ_a^{-1} of a fully active polarization layer grows only as $\mathcal{O}(\mathcal{P}_{(2)})$ to leading order in both models.

Eigenvalues	$\mathcal{P} \ll 1$	$\mathcal{P}_2 \ll 1$
$\lambda_{n_1}^{-1}$	$\mathcal{I}_p^{(2)} \sqrt{\mathcal{P}/2} + 1$	$\sqrt{\mathcal{P}_2/4} + 1$
λ_a^{-1}	$\mathcal{O}(\mathcal{P})$	$\mathcal{O}(\mathcal{P}_2)$
$\lambda_{n_2}^{-1}$	$\mathcal{I}_p^{(1)} \sqrt{\mathcal{P}}$	$\sqrt{\mathcal{P}_2}/2$
$\lambda_{n_3}^{-1}$	$\mathcal{I}_p^{(2)} \sqrt{\mathcal{P}/2} - 1$	$\sqrt{\mathcal{P}_2}/4 - 1$

TABLE I. Behavior of the eigenvalues $\lambda_{n_i}^{-1}$ and λ_a^{-1} for the continuous model (column \mathcal{P}) as well as the 2-species model (column \mathcal{P}_2) for small Péclet numbers.

Hence, up the order $\sqrt{\mathcal{P}_{(2)}}$, the eigenvalue $\lambda_{n_1}^{-1} > \lambda_a^{-1}$. On the other end of the spectrum, for $\mathcal{P}_2 \gg 1$, eigenvalue $\lambda_{n_1}^{-1} \sim \lambda_a^{-1} \sim \sqrt{\mathcal{P}_2}$ for the 2-species model, as can be inferred from Fig. 11 b) and d). The situation is more complicated for the continuous model as can be seen in Fig. 11 a) and c). Depending on the acceptance angle α , $\lambda_{n_1}^{-1}$ can be less or greater than λ_a^{-1} for moderate and

large \mathcal{P} . Choosing $\alpha \equiv \alpha_2 \approx 0.373\pi$, one has $\lambda_{n_1}^{-1} \sim \sqrt{\mathcal{P}}$ for $\mathcal{P} \gg 1$, similar to the 2-species model. For $\alpha \leq \alpha_2$ one has $\lambda_{n_1}^{-1} \leq \lambda_a^{-1}$ for sufficiently large \mathcal{P} . Note however that the limit $\mathcal{P} \gg 1$ must be treated with great caution as the continuous model is based on an approximation (3) that loses its justification for large Péclet numbers (cf. Sec. III C 1). Next, we focus on eigenvalue $\lambda_{n_2}^{-1}$. For both the continuous and the 2-species model, $\lambda_{n_2}^{-1}$ grows proportionally to the square root of the respective Péclet number in the case $\mathcal{P}_{(2)} \ll 1$. As can be inferred from Fig. 11 d), in the limit $\mathcal{P}_2 \rightarrow \infty$, the eigenvalue $\lambda_{n_2}^{-1} \rightarrow 1/\sqrt{2}$ (dashed black line) for the 2-species model. Thus, for infinite activity, the nudging layer decays single-exponentially (since $\lambda_{n_1} \rightarrow 0$) over a characteristic length λ_{n_2} proportional to the extend of a passive layer¹. This limiting behavior becomes intuitively clear since one particle species is instantaneously removed from the nudging region ($\lambda_{n_1} = 0$) while the other species undergoes ordinary diffusion ($\lambda_{n_2} \propto \lambda_p$) until its orientation flips. Regarding the behavior of $\lambda_{n_2}^{-1}$ within the continuous model, we refer to Fig. 11 c). Eigenvalue $\lambda_{n_2}^{-1}$ first seems to approach a constant value close to $1/\sqrt{2}$

as well, but eventually starts to grow again for further increasing \mathcal{P} . Similar to $\lambda_{n_1}^{-1}$, eigenvalue $\lambda_{n_2}^{-1}$ grows proportionally to $\sqrt{\mathcal{P}}$ for $\mathcal{P} \gg 1$. Both eigenvalues differ, however, by 2-3 orders of magnitude in this limit, depending on the choice of the acceptance angle α . We emphasize that the limiting behavior of $\lambda_{n_2}^{-1}$ for $\mathcal{P} \gg 1$ is unphysical. At infinite propulsion speed, particles are instantaneously nudged back to the interface as soon as their orientation lies within the laser's acceptance range. The distance travelled by Brownian motion until properly re-oriented is proportional to $\sqrt{D/D_r}$. Therefore, as for the 2-species model, the nudging layer should decay single-exponentially over said length scale for $\mathcal{P} \rightarrow \infty$. Figure 11 c) shows that the unphysical increase of $\lambda_{n_2}^{-1}$ sets in at $\mathcal{P} \approx 50$ -100, depending on the choice of the acceptance angle α . Finally, the eigenvalue $\lambda_{n_3}^{-1}$ remains negative for all Péclet numbers $\mathcal{P}_{(2)}$ within both models. While approaching the value $-1/\sqrt{2}$ in the limit $\mathcal{P}_2 \rightarrow \infty$ for the 2-species model, $\lambda_{n_3}^{-1}$ approaches zero as $1/\sqrt{\mathcal{P}}$ for $\mathcal{P} \gg 1$ within the continuous model. The behavior of $\lambda_{n_3}^{-1}$ for large Péclet numbers is also unphysical for the same reason as $\lambda_{n_2}^{-1}$.

¹ We remind that lengths are measured in units of the characteristic decay length $\lambda_p = \sqrt{D/(2k)}$ of a passive layer.